Frenkel Exciton Model of Optical Absorption and Photoluminescence in α-PTCDA

I. Vragović[1] and R. Scholz[1]

[1] *Institut für Physik, Technische Universität Chemnitz, D-09107 Chemnitz, Germany*

(Dated: submitted to Phys. Rev. B 30 April 2003, revised version 17 June 2003)

The optical properties of PTCDA (3,4,9,10-perylene-tetracarboxylic-dianhydride) in the monoclinic α-phase are investigated with a model allowing for the transfer of the electronic excitation between different molecular sites in the crystal, resulting from the interactions between the molecular HOMO-LUMO transition dipoles. Due to the large extension of the molecules with respect to the inter-molecular distances, the calculation has to account for the delocalization of the transition charge density over the carbon and oxygen atoms involved in both orbitals. Applying these microscopic ingredients to a calculation of the dispersion of the Frenkel excitons, it can be shown that the dielectric tensor is related to excitons at the Γ point of the Brillouin zone, and the photoluminescence to vertical recombination starting from the minimum of the Frenkel exciton dispersion at the surface of the Brillouin zone. The calculated results agree both with the extinction coefficient measured on poly-crystalline thin films and with the dominating low-temperature photoluminescence decay channel observed on single crystals of α-PTCDA.

PACS numbers: PACS numbers: 71.35.Aa, 78.55.Kz, 71.35.Cc, 78.20.Bh

I. INTRODUCTION

Thin films and multilayers of crystalline organic dyes with semiconducting properties like polyacenes, thiophenes and perylene derivates have attracted enormous interest because of various applications like organic light-emitting devices [1], solar cells [2], and field effect transistors [3]. The optical and electronic properties of these organic materials are determined both by the strong covalent bonds within each molecule and by the much weaker electric multipole and van-der-Waals interactions between different molecular sites.

Recent advances in organic molecular beam deposition have allowed for the fabrication of abrupt and clean organic hetero-interfaces of different molecular materials [4]. Among the many organic molecules studied in the past decade, much work has been focused on 3,4,9,10-perylene-tetracarboxylic-dianhydride (PTCDA). As this substance forms two monoclinic centro-symmetric crystal phases of space group $P2_1/c$ (C_{2h}^5) with two nearly coplanar molecules per unit cell, it grows on a large variety of non-reactive substrates with the molecules of the first monolayer lying flat on the substrate surface [4, 5]. Films deposited with organic molecular beam deposition at room temperature are usually dominated by the α-phase, whereas the β-phase grows preferentially at low substrate temperatures [6, 7]. As most spectroscopic investigations concerned α-PTCDA, the present work will focus on this crystalline phase, cp. Fig. 1. The distance between consecutive molecular planes is shorter than in non-polar materials like graphite or perylene, resulting in a large overlap of the molecular π-orbitals. The electronic interaction between the two different molecules in the unit cell is expected to be much smaller, leading e.g. to a large anisotropy of the mobility [8]. However, from the geometry of the molecules in the crystal phase determined by X-ray diffraction [5] and electron diffraction [9], it is obvious that the steric hindrance between the

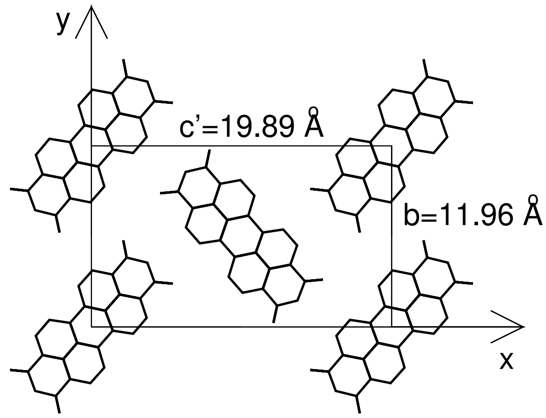

FIG. 1: Crystal unit cell of α-PTCDA, in the plane most closely coinciding with the molecular planes, where $\mathbf{c}'$ corresponds to the ($\mathbf{c} - 2\ \mathbf{a}$) direction of the published crystal basis vectors [5]. The HOMO-LUMO transition dipoles of the two basis molecules at $\mathbf{r}_A = \mathbf{0}$ and at $\mathbf{r}_B = (\mathbf{b} + \mathbf{c}')/2$ are oriented along the long axes of the molecules forming an angle of $\varphi = 50.4^0$ with $\mathbf{c}'$, and in the following we will use the convention that they point upwards. The molecular stacks develop along the third lattice vector, oriented along $\mathbf{a} = a(\cos\beta', 0, \sin\beta')$, with $a = 3.72$ Å and $\beta' = 120.5^0$. The distance between consecutive planes is $d = a\sin\beta' = 3.205$ Å.

oxygen and hydrogen atoms of the two basis molecules leads to deviations from the rectangular D_{2h} symmetry expected for the free molecule.

The optical properties in the crystalline phase are influenced by the deformation of an effective internal vibrational mode in the relaxed excited geometry of a single molecule, and by transfer of Frenkel excitons between different molecular sites in the crystal. Moreover, due to the small inter-molecular separation, completely different types of optical excitations like charge transfer (CT) excitons can appear.

The first model proposed for the optical properties of crystalline PTCDA films applied the concept of three-dimensional Wannier-Mott excitons to optical absorption, time-resolved photoluminescence [10] and electro-absorption [11] in organic quantum-well structures. This approach resulted in an excitonic Bohr radius of 12 Å, indicating that the excitonic wave function extends over a few molecular layers in PTCDA. In organic heterostructures, the dependence of the optical properties on the quantum well width was analysed in terms of the confinement of Wannier-like excitons, resulting in a disk-like deformation of the excitonic wave function [10]. However, there seems to be no microscopic foundation for the key assumption of these Wannier exciton models: Nearly isotropic band masses. Therefore, subsequent approaches abandoned this close analogy with inorganic semiconductors and developed microscopic models accounting for the localized character of the molecular orbitals and the resulting electronic transitions, expressed in terms of neutral Frenkel excitons and CT excitons involving two neighbouring molecules. Such molecular concepts were applied to absorption of dissolved PTCDA, thin film absorption and fluorescence, exciton diffusion in thin films and electro-absorption [4, 12, 13]. Within the framework of non-interacting Frenkel and CT excitons, the transition at 2.23 ± 0.03 eV in the crystalline phase was assigned to a CT state, exhibiting effects of quantum confinement [10] in heterostructures.

An interpretation of PTCDA excitations as mixed Frenkel and CT states, each with its vibronic replicas, was proposed in a dimer model [14, 15]. A possible contribution of CT excitons to PTCDA absorption and electro-absorption in terms of an exciton-phonon-CT dimer was analysed and compared with the observed absorption and emission in PTCDA films and multiple quantum wells [15]. The main lack of this model is that it does not account for the periodicity of the practically infinite real crystal structure. As a consequence, the dimer model fails to develop the full concept of excitons as propagating collective crystal excitations in $\mathbf{k}$-space, giving a questionable estimate for the Γ point of the exciton dispersion, where actually the absorption takes place.

Further developments adjusted this approach to the infinite one-dimensional stack geometry including Frenkel excitons with several vibronic levels and CT excitons. Assuming a large intermolecular π-orbital-overlap between nearest neighbours, the nature of the lowest transition at the Γ-point of the first Brillouin zone was interpreted by a mixing of Frenkel and CT excitations [16]. An additional complication arises from the fact that the deformation in the relaxed excited state of a monomer spreads into a deformation cloud surrounding the optically excited molecule in the crystal. A one-dimensional Holstein model [17] can account for this spreading of the deformation around the excited molecule, and as a consequence, the higher vibronic levels in the excited state of the molecules split into various sub-peaks, whereas the lowest vibronic level is only influenced energetically [18].

Albeit all of these model calculations accounted for a possible CT exciton, none included the full crystal geometry with two molecules in the unit cell. Recently, a theoretical investigation based on a realistic crystal geometry has been performed, including the deformation of an effective internal vibration, the Frenkel exciton, and three types of CT excitons [19]. In the parameter set used in these calculations, the CT energies were placed *above* the lowest vibronic level of the Frenkel exciton, so that a mixing of both types of excitations by electron and hole transfer integrals influences on details of the absorption and electro-absorption lineshapes [19]. On the other hand, from investigations of molecular dimers with time-dependent density functional techniques, the resulting CT energies were found *below* the Frenkel exciton [20], and with some realistic modifications of the geometries of the relaxed excited dimers, these CT transition energies agree with the CT bands observed with time-resolved luminescence techniques [21, 22]. As these estimates for the CT energies are below the Frenkel exciton, the mixing of both types of excitons by electron and hole transfer is not expected to influence strongly on the absorption lineshape. Independently from the scatter of the CT energies obtained with different approaches, their oscillator strength with respect to the Frenkel excitons was found to be rather low in all cases: The ratio of the transition dipoles was estimated to be 0.14 [16] and 0.15 [19], resulting in a relative oscillator strength of about 2 - 3 %, similar to the value obtained with time-dependent density functional theory for dimers [23].

From these low transition dipole moments of the CT states, it is obvious that they influence only weakly on the strength of the optical absorption, and, depending on the precise value of their energies and the electron and hole transfer parameters, they can at most deform the lineshape defined mainly by the Frenkel exciton transition. Therefore, it is a relevant issue to fix all the microscopic parameters needed in a pure Frenkel exciton picture before attempting to address the complications arising from the mixing with the CT states.

In this work, we present such a pure Frenkel exciton model, including microscopic calculations of the transfer of the neutral excitation between different molecular sites. The proposed method has already been applied to the linear optical properties [23–25] and to low-temperature photoluminescence in single crystals of α-PTCDA [21, 26], but some of the microscopic ingredients were not discussed in great detail. Before developing this model approach, we would like to stress again its key approximations: Neglect of all CT states because we expect their energies below the Frenkel exciton [20], and neglect of the spreading of the deformation cloud [18] around the excited molecular site.

In Sec. II, we define the ground and the optically excited state of the molecular crystal and perform a block diagonalization of the Frenkel exciton Hamiltonian. The calculation of the exciton transfer energies, where the transition dipoles are replaced by distributions of overlap charges, and the comparison with the point-dipole approximation are given in Sec. III. Sec. IV is devoted to the calculation of transition dipole moments and the anisotropic dielectric tensor, including a detailed comparison with available experimental data for poly-crystalline thin films [24]. In Sec. V, we extend our microscopic model to the $\mathbf{k}$-space dispersion of the Frenkel excitons. Sec. VI is devoted to the calculation of the photoluminescence (PL) out of the minimum of the exciton dispersion found in Sec. V, and the results are compared to recent low-temperature time-resolved PL data [21]. The achievements and limits of the present approach are summarized in Sec. VII.

II. MODEL HAMILTONIAN FOR OPTICAL EXCITATION

In the following, we assume that the high-frequency internal vibrations elongated in the relaxed excited state of a PTCDA molecule [27] can be replaced by a single *effective* internal mode of $\hbar\omega_{\rm eff} = 0.17$ eV, corresponding to the energy difference between consecutive vibronic subbands in the optical absorption of dissolved molecules [6, 12, 28]. According to the Franck-Condon principle, the molecular geometry is conserved on the time scale of the electronic transition. The distribution of geometries in the lowest vibronic level in the electronic ground state is then reflected in Franck-Condon overlap factors $S_{\nu_e 0_g} = \langle \chi^{e\nu_e} | \chi^{g0_g} \rangle$ with the vibronic levels of the electronic excited state. Their square gives the relative contribution of different vibronic sublevels to the optical excitation of the monomer:

$$S^2_{\nu_e 0_g} = \langle \chi^{e\nu_e} | \chi^{g0_g} \rangle^2 = e^{-g^2} \frac{g^{2\nu_e}}{\nu_e!} = P_{\nu_e}(g^2), \qquad (1)$$

following a Poisson progression P_{ν_e} with argument g^2. Previous estimates for the exciton-vibrational coupling constant g^2 range from 0.67 for dissolved PTCDA [15] to a calculated value of 1.18 for the isolated molecule [27, 29], which is a realistic value for matrix-isolated PTCDA molecules with an infrared dielectric constant of the matrix material close to unity in the energy region of the internal vibrational modes [30]. Compared to polar solvents, we expect a weaker dielectric influence of the surrounding PTCDA crystal, so that we assume in the following a value of $g^2 = 1.0$, somewhat closer to the value calculated for the free molecule. The influence of the choice of g^2 on other material parameters will be addressed again in Sec. VII.

Within this effective mode model, we can factorize the electronic ground state of the crystalline phase into the product of the ground state wave functions of the constituting molecules:

$$|g\rangle = \prod_{\mathbf{n}\alpha} |\phi^g_{\mathbf{n}\alpha} \chi^{g0_g}_{\mathbf{n}\alpha}\rangle = \prod_{\mathbf{n}\alpha} |\mathbf{n}\alpha 0_g\rangle, \qquad (2)$$

where $\phi^g_{\mathbf{n}\alpha}$ is the electronic wave function in the ground state of molecule $\alpha \in \{A, B\}$ in unit cell $\mathbf{n}$, and $\chi^{g0_g}_{\mathbf{n}\alpha}$ its lowest vibronic eigenstate. For brevity, in the last expression, the ϕ and χ characterizing the electronic and vibronic part of the product wave function have been skipped.

Due to the large value of the exciton-phonon coupling constant, we assume that both the basis for the electronic transition and the internal molecular vibration reside on the same molecule [16], neglecting any configuration in which they are placed on different molecular sites [17, 18, 31]. Within this approximation, the above factorized ground state $|g\rangle$ allows to analyse optical excitations in terms of localized molecular transitions towards vibronic eigenstates associated to the excited electronic state:

$$b^+_{\mathbf{n}\alpha\nu_e;\mathbf{n}\alpha 0_g} |\phi^g_{\mathbf{n}\alpha} \chi^{g0_g}_{\mathbf{n}\alpha}\rangle = |\phi^e_{\mathbf{n}\alpha} \chi^{e\nu_e}_{\mathbf{n}\alpha}\rangle, \qquad (3)$$

where $\phi^e_{\mathbf{n}\alpha}$ is the electronic part of the wave function in the electronically excited state, and $\chi^{e\nu_e}_{\mathbf{n}\alpha}$ the ν_eth vibronic state in the excited state potential. Even though in eq. (3) the molecule α in unit cell $\mathbf{n}$ before and after excitation is the same, the use of two complete sets of 3 indices on the exciton creation operator will become useful later on, especially for the calculation of the PL spectra in Sec. VI. The excited state of the whole crystal corresponding to eq. (3) can again be factorized,

$$\begin{aligned} b^+_{\mathbf{n}\alpha\nu_e;\mathbf{n}\alpha 0_g} |g\rangle &= |\phi^e_{\mathbf{n}\alpha} \chi^{e\nu_e}_{\mathbf{n}\alpha}\rangle |\phi^g_{\mathbf{n}\beta} \chi^{g0_g}_{\mathbf{n}\alpha}\rangle \\ &\times \prod_{\mathbf{m}\neq\mathbf{n}} |\phi^g_{\mathbf{m}\alpha} \chi^{g0_g}_{\mathbf{m}\alpha}\rangle |\phi^g_{\mathbf{m}\beta} \chi^{g0_g}_{\mathbf{m}\alpha}\rangle, \end{aligned} \qquad (4)$$

where $\beta \neq \alpha$. These product states are at the basis of our formulation of the Frenkel exciton Hamiltonian in Heitler-London approximation [32, 33]. For the model system PTCDA, the exciton Hamiltonian for the three-dimensional molecular crystal with two molecules per unit cell reads [25]:

$$\begin{aligned} H^e &= \sum_{\mathbf{n}} \sum_{\alpha=A,B} \sum_{\nu_e} E_{0_g\nu_e} b^+_{\mathbf{n}\alpha\nu_e;\mathbf{n}\alpha 0_g} b_{\mathbf{n}\alpha\nu_e;\mathbf{n}\alpha 0_g} \\ &+ \sum_{\mathbf{n}\alpha\nu_e} \sum_{\mathbf{m}\beta\mu_e} t_{\mathbf{n}\alpha\nu_e;\mathbf{m}\beta\mu_e} b^+_{\mathbf{n}\alpha\nu_e;\mathbf{n}\alpha 0_g} b_{\mathbf{m}\beta\mu_e;\mathbf{n}\beta 0_g}, \end{aligned} \qquad (5)$$

where $E_{0_g\nu_e} = E_{0_g 0_e} + D + \nu_e \hbar\omega_{\rm eff}$ is the exciton on-site energy in the ν_eth vibronic level, composed of the transition energy $E_{0_g 0_e} \approx 2.60$ eV between the lowest vibronic levels $|\chi^{g0_g}_{\mathbf{n}\alpha}\rangle$ and $|\chi^{e0_e}_{\mathbf{n}\alpha}\rangle$ of the free molecule [34], an environment-dependent shift D adjusted to the observed transition energy in the crystalline phase [32], and a vibronic part. The above Hamiltonian H^e applies to the Frenkel exciton states in eq. (4) excited out of the ground state $|g\rangle$ in eq. (2) with one of the exciton creation operators in eq. (3). Therefore, these single exciton states are still referring to a crystal ground state without any electronic or vibronic excitation.

As we neglect any spreading of the deformation cloud around the excited molecule [18], the transfer matrix element $t_{\mathbf{n}\alpha\nu_e;\mathbf{m}\beta\mu_e}$ has to return the molecule β in unit cell

$\mathbf{m}$ into the lowest vibronic level of the electronic ground state, while the molecule α in unit cell $\mathbf{n}$ is promoted into an excitonic state in the vibronic sublevel ν_e of the excited state potential. For this reason, the transfer matrix elements can be decomposed into an electronic and a vibronic part,

$$t_{\mathbf{n}\alpha\nu_e;\mathbf{m}\beta\mu_e} = T_{\mathbf{n}\alpha;\mathbf{m}\beta} S_{\nu_e 0_g} S_{\mu_e 0_g}, \tag{6}$$

where $S_{\nu_e 0_g}$ and $S_{\mu_e 0_g}$ are the vibronic Franck-Condon factors as in eq. (1). As usual in periodic systems [35], it is convenient to perform a total Fourier transformation into wave-vector representation

$$b^+_{\mathbf{k}_e\alpha\nu_e} = \frac{1}{\sqrt{N}} \sum_{\mathbf{n}} e^{-i\mathbf{k}_e\cdot\mathbf{R}_{\mathbf{n}\alpha}} b^+_{\mathbf{n}\alpha\nu_e;\mathbf{n}\alpha 0_g}, \tag{7}$$

where $\mathbf{R}_{\mathbf{n}\alpha} = \mathbf{R}_{\mathbf{n}} + \mathbf{r}_\alpha$ is the position of the α molecule in the crystal unit cell $\mathbf{n}$.

The ground state with its vanishing momentum $\mathbf{k}_g = \mathbf{0}$ is the same for all excitations at a certain wave vector $\mathbf{k}_e$, so that all indices referring to it will be omitted in the following calculations concerning the linear optical properties of α-PTCDA. However, in the calculations of the PL spectra in Sec. VI, we shall introduce vibronically excited levels of the electronic ground state after recombination, so that the corresponding indices will become meaningful again.

The Fourier transform results in a decoupling of the Hamiltonian into independent sub-blocks for different wave vectors:

$$\begin{aligned} H^e(\mathbf{k}_e) &= \sum_{\alpha\nu_e} E_{0_g\nu_e} b^+_{\mathbf{k}_e\alpha\nu_e} b_{\mathbf{k}_e\alpha\nu_e} \\ &+ \sum_{\alpha\nu_e,\beta\mu_e} S_{\nu_e 0_g} S_{\mu_e 0_g} T_{\alpha\beta}(\mathbf{k}_e) b^+_{\mathbf{k}_e\alpha\nu_e} b_{\mathbf{k}_e\beta\mu_e}, \end{aligned} \tag{8}$$

where

$$T_{\alpha\beta}(\mathbf{k}_e) = \sum_{\mathbf{R}_{\mathbf{n}\alpha;\mathbf{m}\beta}\neq 0} e^{-i\mathbf{k}_e\cdot\mathbf{R}_{\mathbf{n}\alpha;\mathbf{m}\beta}} T_{\mathbf{n}\alpha;\mathbf{m}\beta} \tag{9}$$

with $\mathbf{R}_{\mathbf{n}\alpha;\mathbf{m}\beta} = \mathbf{R}_{\mathbf{n}\alpha} - \mathbf{R}_{\mathbf{m}\beta}$ is the discrete Fourier transform of the transfer matrix element, summed over the relative positions of the molecules β in unit cell $\mathbf{m}$ with respect to the reference molecule α in unit cell $\mathbf{n}$. Because the PTCDA crystal has a center of inversion, the exciton transfer matrix elements $T_{\alpha\beta}(\mathbf{k}_e)$ are real and symmetric about the indices α and β [32].

For each wave vector, the Hamiltonian (8) has the form of a block matrix:

$$H^e(\mathbf{k}_e) = \begin{pmatrix} H^e_{AA}(\mathbf{k}_e) & H^e_{BA}(\mathbf{k}_e) \\ H^e_{AB}(\mathbf{k}_e) & H^e_{BB}(\mathbf{k}_e) \end{pmatrix}, \tag{10}$$

where the block $H^e_{AA}(\mathbf{k}_e)$ stands for the transfer of the optical excitation from a basis molecule A to all A molecules in the other unit cells, and similarly for the other entries. The different blocks have the following structure concerning the vibronic levels ν_e, μ_e:

$$\begin{aligned} H^e_{AA;\nu_e\mu_e}(\mathbf{k}_e) &= H^e_{BB;\nu_e\mu_e}(\mathbf{k}_e) & (11)\\ &= E_{0_g\nu_e}\delta_{\nu_e\mu_e} + S_{\nu_e 0_g} S_{\mu_e 0_g} T_{AA}(\mathbf{k}_e), \\ H^e_{AB;\nu_e\mu_e}(\mathbf{k}_e) &= H^e_{BA;\nu_e\mu_e}(\mathbf{k}_e) & (12)\\ &= S_{\nu_e 0_g} S_{\mu_e 0_g} T_{AB}(\mathbf{k}_e). \end{aligned}$$

In the following, we will use the abbreviations $X(\mathbf{k}_e) = T_{AA}(\mathbf{k}_e)$ and $V(\mathbf{k}_e) = T_{AB}(\mathbf{k}_e)$. As the Hamiltonian (10) is invariant under exchange of the two basis molecules A $\leftrightarrow$ B, all eigenstates must have a well-defined parity with respect to this operation. After a rotation into such a basis, the Hamiltonian is block-diagonalized:

$$H^e(\mathbf{k}_e) = \begin{pmatrix} H^e_{AA}(\mathbf{k}_e) + H^e_{AB}(\mathbf{k}_e) & 0 \\ 0 & H^e_{AA}(\mathbf{k}_e) - H^e_{AB}(\mathbf{k}_e) \end{pmatrix}. \tag{13}$$

where the upper and lower blocks are related to the excitations

$$b^+_{\mathbf{k}_e x_e\nu_e} = \frac{1}{\sqrt{2}}\left(b^+_{\mathbf{k}_e A\nu_e} - b^+_{\mathbf{k}_e B\nu_e}\right) \tag{14}$$

and

$$b^+_{\mathbf{k}_e y_e\nu_e} = \frac{1}{\sqrt{2}}\left(b^+_{\mathbf{k}_e A\nu_e} + b^+_{\mathbf{k}_e B\nu_e}\right), \tag{15}$$

respectively, with the indices x_e or y_e referring to the orientation of their dipole moment in the cartesian coordinate system of Fig. 1. The Hamiltonian (13) can be diagonalized by a unitary transformation with respect to the vibronic sublevels, resulting in excitations

$$b^+_{\mathbf{k}_e\gamma_e\eta_e} = \sum_{\nu_e} u_{\nu_e,\gamma_e\eta_e}(\mathbf{k}_e) b^+_{\mathbf{k}_e\gamma_e\nu_e} \tag{16}$$

for $\gamma_e = x_e, y_e$ where the vibronic sublevel η_e for the excitons arises from the diagonalization of the sub-blocks of (13) and the corresponding eigenvectors $u_{\nu_e,\gamma_e\eta_e}(\mathbf{k}_e)$. The diagonalization of the Hamiltonian and the calculation of the eigenvalues and eigenvectors are carried out numerically.

III. MICROSCOPIC ESTIMATES FOR EXCITON TRANSFER ENERGIES

Due to the small wave vector of the photon, the calculation of the linear optical properties in Sec. IV can be performed at the Γ point of the Brillouin zone, where the plane waves in the discrete Fourier transform in eq. (9) can be skipped. Therefore, in the present Section, the discussion of the exciton transfer will be restricted to the Γ point, but generalizations to the exciton dispersion will be investigated in Sec. V.

For a sufficient distance between the molecular sites, the exciton transfer integrals $T_{\mathbf{n}\alpha;\mathbf{m}\beta}$ can be estimated by the interaction between the transition dipoles $\mathbf{d}_\alpha$, $\mathbf{d}_\beta$ [32, 36]. In point-dipole approximation, it has the following form:

$$T_{\mathbf{n}\alpha;\mathbf{m}\beta}(\mathbf{r}) = \frac{1}{4\pi\epsilon_0\epsilon(\mathbf{r})\mathbf{r}^5} \times \left[(\mathbf{d}_\alpha\cdot\mathbf{d}_\beta)\,\mathbf{r}^2 - 3\,(\mathbf{d}_\alpha\cdot\mathbf{r})\,(\mathbf{d}_\beta\cdot\mathbf{r})\right] \tag{17}$$

where $\mathbf{r} = \mathbf{R}_{\mathbf{n}\alpha;\mathbf{m}\beta}$ is the difference between the positions of molecule α in unit cell $\mathbf{n}$ and molecule β in unit cell $\mathbf{m}$. This point-dipole approach is only applicable for an isotropic dielectric constant ϵ and for distances much larger than the spatial extension of a molecule. In the following, we use it for an estimate of the exciton transfer to more distant molecules in the unscreened case ($\epsilon = 1$).

As discussed for other conjugated materials, a supermolecular approach and exciton coupling through the electrostatic interaction between the atomically resolved transition densities give largely equivalent results, whereas the point-dipole approximation of the transition dipoles is rather crude [37]. In order to investigate the delocalized nature of the transition dipole, we express the HOMO and LUMO π wave functions as sums of localized atomic-like basis states [27]:

$$\begin{aligned}\Phi_{HOMO}(\mathbf{r}) &= \sum_i a_i\Phi_z(\mathbf{r}-\mathbf{R}_i)\\ \Phi_{LUMO}(\mathbf{r}) &= \sum_j b_j\Phi_z(\mathbf{r}-\mathbf{R}_j)\end{aligned} \tag{18}$$

From this decomposition, it becomes clear that the transition charge density is extended over the whole molecule,

$$\begin{aligned}&\langle\Phi_{LUMO}(\mathbf{r})|e\mathbf{r}|\Phi_{HOMO}(\mathbf{r})\rangle\\ &= \sum_{i,j} eb_j^* a_i\langle\Phi_z(\mathbf{r}-\mathbf{R}_j)|\mathbf{r}|\Phi_z(\mathbf{r}-\mathbf{R}_i)\rangle\\ &= \sum_i eb_i^* a_i\mathbf{R}_i\ \ (+\text{ terms with } i\neq j),\end{aligned} \tag{19}$$

resulting in a distribution of transition charges $q_i = eb_i^* a_i$ over the heavy atoms of the molecule, cp. Fig. 2. For the calculation of the exciton transfer, we neglect all non-diagonal terms ($i \neq j$), so that we can replace the transition dipoles by a distribution of charges q_i localized on the atomic sites. In this approximation, the interaction of two extended molecular transition dipoles is replaced by the interaction between two distributions of point charges on each molecule. For the anisotropic dielectric medium, we assume the static dielectric tensor to be diagonal in the coordinate system of Fig. 1, with values $\epsilon_\parallel = \epsilon_{xx} = \epsilon_{yy} = 4.07$ and $\epsilon_\perp = \epsilon_{zz} = 1.85$ [38]. The resulting interaction reads [39]:

$$T_{\mathbf{n}\alpha;\mathbf{m}\beta} = \frac{1}{4\pi\epsilon_0\sqrt{\epsilon_{xx}\epsilon_{yy}\epsilon_{zz}}} \times \sum_{i,j}\frac{q_{i\alpha}q_{j\beta}}{\left[\frac{x^2_{i\alpha,j\beta}}{\epsilon_{xx}}+\frac{y^2_{i\alpha,j\beta}}{\epsilon_{yy}}+\frac{z^2_{i\alpha,j\beta}}{\epsilon_{zz}}\right]^{1/2}} \tag{20}$$

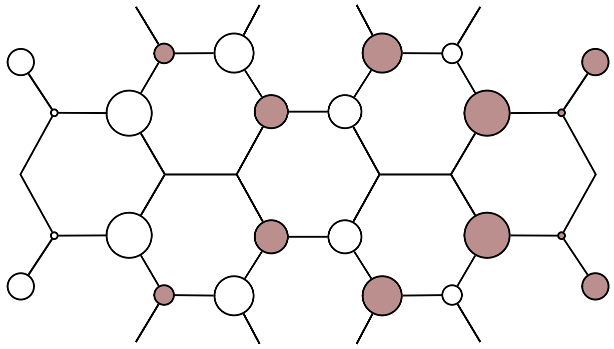

FIG. 2: Distribution of the transition density $\Phi^*_{LUMO}(\mathbf{r})\Phi_{HOMO}(\mathbf{r})$ over a PTCDA molecule, calculated with density functional tight-binding techniques [27]. The area of the circles corresponds to the relative contribution of the different atoms, and gray and white circles symbolize opposite signs. The resulting transition dipole moment is oriented along the long axis of the molecule.

where $q_{i\alpha}$ and $q_{j\beta}$ are the transition charges of the i-th atom in the molecule α and the j-th atom in the molecule β, respectively, and $x_{i\alpha,j\beta} = x_{i\alpha} - x_{j\beta}$, etc. are the components of the spatial separation between these two atoms. This inclusion of the dielectric tensor of the organic crystal in the calculation of the atomically resolved interacton between the transtion dipole moments is a generalization of previous approaches [37]. The overall scaling of the transition charge density is determined by a value of $d_0 = 6.45$ Debye for the HOMO-LUMO transition dipole which is fitted to the measured absorption coefficient, cp. Sec. IV.

For inorganic semiconductors, it was found that the dielectric constant of the bulk develops on a length scale corresponding to the distance between neighbouring atoms [40]. Generalized to the present case of a strongly anisotropic system, it can be assumed that the full screening applies to the interaction between two molecules whose separation exceeds the lattice unit vectors, but for pairs of neighbouring molecules, the dielectric screening is likely to be reduced.

For later reference, we divide the exiton transfer to all *equivalent* molecules into two parts:

$$\begin{aligned}X(\mathbf{k}_e) = T_{AA}(\mathbf{k}_e) &= \sum_{\mathbf{R}_{\mathbf{n}A;\mathbf{m}A}\neq 0} T_{\mathbf{n}A;\mathbf{m}A}\, e^{-i\mathbf{k}_e\cdot\mathbf{R}_{\mathbf{n}A;\mathbf{m}A}}\\ &= 2W(\mathbf{k}_e) + M(\mathbf{k}_e),\end{aligned} \tag{21}$$

where the sum M denotes the transfer to all equivalent molecules in different unit cells except for the stack neighbours, and W the transfer to each of these neighbouring molecules.

For the exciton transfer to the stack neighbours, the assumed screening model is most crucial, because the dielectric constant of the bulk develops on a length scale corresponding to the distance between neighbouring atoms [40], which in this case is given by the stacking distance. For unscreened interaction with $\epsilon = 1$, a transition dipole of $d_0 = 6.45$ Debye results in $W(\mathbf{0}_e) = 94$ meV, whereas for the bulk values of the anisotropic dielectric tensor, the exciton transfer to the stack neighbour is strongly reduced to $W(\mathbf{0}_e) = 21$ meV. A more precise estimate would require a generalization of the Thomas-Fermi screening model [40] to an anisotropic dielectric surrounding, which is beyond the scope of the present work. From the analysis of the experimental extinction coefficient in the next Sec., we find a value of $W(\mathbf{0}_e) = 82$ meV, within the range defined by the microscopic calculations for the fully screened and unscreened cases.

In the following, we assume that the crystallites in the epitaxial film have a finite size, so that the non-analyticity problems of the sums in eqs. (9,21) arising for an infinite crystal at $\mathbf{k}_e = \mathbf{0}$ [32] disappear. Performing the summations over crystallites corresponding to spheres in terms of crystal unit cells, i.e. ellipsoids in real space, we can compute the size dependence of the transfer sums, cp. Fig. 3. Both for the fully screened ($\epsilon_\parallel = 4.07$ and $\epsilon_\perp = 1.85$) and the unscreened case with $\epsilon = 1$, M and V are mainly determined by the largest interactions in the immediate surroundings of the reference molecule, so that the dependence on the interaction range is quite weak beyond about 5 unit cells. Even though the point-dipole approximation is much cruder, we still observe a qualitatively similar dependence of the exciton transfer sums on the interaction radius, cp. Fig. 3. However, the cancellation of the contributions of molecules in different directions around the reference molecule is less efficient, so that a small dependence on crystallite size remains even for large radius R. Asymptotically, it behaves like $\log R$, as expected from an integration of the $1/r^3$ dependence in eq. (17).

Interestingly, in the atomically resolved calculation based on a realistic anisotropic dielectric tensor, this logarithmic singularity has a nearly vanishing prefactor. Therefore, we suppose that this term should cancel exactly, so that details of the unit cell geometry and the values of the dielectric tensor elements result in a finite value for the Frenkel exciton transfer at the Γ point of the Brillouin zone.

Assuming full screening even for the immediate surroundings of the reference molecule, the asymptotic value of the A $\leftrightarrow$ B transfer would be $V(\mathbf{0}_e) = 34$ meV, below the value of $V(\mathbf{0}_e) = 47$ meV deduced from the comparison with the experimental absorption coefficient [24] in Sec. IV. Therefore, we assume that for the transfer matrix elements to the 12 closest inequivalent neighbours the dielectric screening should be reduced to a value between $\epsilon = 1$ and the bulk value of the diectric tensor. For simplicity, we multiply all 12 transfer matrix elements to the corresponding molecules at the distances 10.53 Å, 11.60 Å and 13.64 Å from the reference site with the same prefactor of 1.37 with respect to the fully screened case, cp. the solid line for V in Fig. 3. The four coplanar inequivalent neighbouring molecules visualized in Fig. 1 contribute about one half of the total transfer matrix element $V(\mathbf{0}_e)$, and each of the two surrounding layers about one quarter.

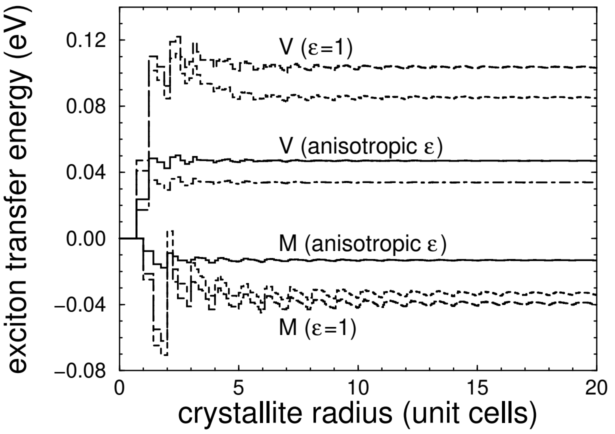

FIG. 3: Exciton transfer energies $M(\mathbf{0}_e)$ and $V(\mathbf{0}_e)$ at the Γ point of the Brillouin zone, calculated with atomically resolved HOMO-LUMO transition dipole moments for different models of the dielectric tensor. The sums of the transfer matrix elements are performed over spheres in terms of unit cells, or ellipsoids in real space, whose radius is reported on the abscissa. Long dashes: unscreened isotropic medium with $\epsilon = 1$; short dashes: point-dipole approximation for $\epsilon = 1$. For the experimental values of the dielectric tensor, $\epsilon_\parallel = 4.07$ and $\epsilon_\perp = 1.85$, we obtain an asymptotic value of $M(\mathbf{0}_e) = -14$ meV (solid line) and $V(\mathbf{0}_e) = 34$ meV (dash-dotted). According to the fit to the measured absorption coefficient in Sec. IV, the asymptotic value of V should be $V(\mathbf{0}_e) = 47$ meV (solid line), which has been obtained with a reduced dielectric screening for the transfer matrix elements involving the 12 closest inequivalent neighbouring molecules (solid line).

IV. TRANSITION DIPOLE MOMENTS AND DIELECTRIC TENSOR

For a given set of microscopic transfer parameters $X(\mathbf{0}_e)$ and $V(\mathbf{0}_e)$, the diagonalization of the Hamiltonian (13) results in transition energies $E_{\mathbf{0}_e x_e \eta_e}$ and $E_{\mathbf{0}_e y_e \eta_e}$ and the corresponding excitonic eigenstates at the Γ point of the Brillouin zone. The transition dipole moments of these states,

$$\mathbf{d}_{\mathbf{0}_e x_e \eta_e} = \langle g | e\mathbf{r} | b^+_{\mathbf{0}_e x_e \eta_e} g \rangle \tag{22}$$

and

$$\mathbf{d}_{\mathbf{0}_e y_e \eta_e} = \langle g | e\mathbf{r} | b^+_{\mathbf{0}_e y_e \eta_e} g \rangle, \tag{23}$$

respectively, can be expressed in terms of the transition dipole moments of the vibronic sublevels of the molecular excitations $\langle g | e\mathbf{r} | b^+_{\mathbf{n}\alpha\nu_e} g \rangle = \langle \phi^g_{\mathbf{n}\alpha} | e\mathbf{r} | \phi^e_{\mathbf{n}\alpha} \rangle \langle \chi^{g0_g}_{\mathbf{n}\alpha} | \chi^{e\nu_e}_{\mathbf{n}\alpha} \rangle = \mathbf{d}_\alpha S_{\nu_e 0_g}$,

$$\mathbf{d}_{\mathbf{0}_e x_e \eta_e} = \sqrt{\frac{N}{2}} (\mathbf{d}_A - \mathbf{d}_B) \sum_{\nu_e} u_{\nu_e, x_e \eta_e}(\mathbf{0}_e) S_{\nu_e 0_g} \tag{24}$$

and

$$\mathbf{d}_{\mathbf{0}_e y_e \eta_e} = \sqrt{\frac{N}{2}} \left(\mathbf{d}_A + \mathbf{d}_B\right) \sum_{\nu_e} u_{\nu_e, y_e \eta_e}(\mathbf{0}_e) S_{\nu_e 0_g}, \quad (25)$$

where the total coupling strength $\sum_{\eta_e}(|\mathbf{d}_{\mathbf{0}_e x_e \eta_e}|^2 + |\mathbf{d}_{\mathbf{0}_e y_e \eta_e}|^2) = N(\mathbf{d}_A^2 + \mathbf{d}_B^2)$ is conserved by the unitary transformation to the excitonic eigenstates.

Assuming a finite damping rate Γ_η for each transition, the diagonal elements of the dielectric tensor in the xy plane of Fig. 1 can be expressed as a sum over Lorentzian lineshapes:

$$\begin{aligned} \epsilon_{xx}(\omega) &= 1 + \chi_b(\omega) + \frac{2}{\epsilon_0 V \hbar} \sum_{\eta_e} \mathbf{d}^2_{\mathbf{0}_e x_e \eta_e} \quad (26) \\ &\times \left[\frac{1}{\omega_{\mathbf{0}_e x_e \eta_e} - \omega - i\Gamma_{\eta_e}} + \frac{1}{\omega_{\mathbf{0}_e x_e \eta_e} + \omega + i\Gamma_{\eta_e}} \right], \end{aligned}$$

and similarly for $\epsilon_{yy}(\omega)$, where $\omega_{\mathbf{0}_e x_e \eta_e} = E_{\mathbf{0}_e x_e \eta_e}/\hbar$ are the transition frequencies, $\chi_b(\omega)$ a frequency-dependent background stemming from higher-lying transitions, V the crystal volume, and the factor of 2 accounts for spin degeneracy. The above dielectric function is equivalent to the following oscillator strengths of the vibronic sub-levels:

$$F_{\mathbf{0}_e \gamma_e \eta_e} = \frac{2m\omega_{\mathbf{0}_e \gamma_e \eta_e} \mathbf{d}^2_{\mathbf{0}_e \gamma_e \eta_e}}{e^2 \hbar} \quad (27)$$

for the two polarization directions $\gamma_e = x_e, y_e$. As discussed previously, the Lorentzian lineshapes in eq. (26) result in too extended tails of the absorption features, a deficiency which can be cured by using modified Lorentzian lineshapes resulting in small deviations from Kramers-Kronig consistency [24, 41]. Instead of this approach, we apply a Kramers-Kronig consistent lineshape based on Gaussian broadenings for the imaginary parts [41–43]. Based on infinitesimal dephasings Γ_{η_e} and normalized Gaussians

$$G(\omega', \omega_{\mathbf{0}_e x_e \eta_e}, \sigma_{\eta_e}) = \frac{1}{\sqrt{2\pi}\sigma_{\eta_e}} e^{-\frac{(\omega' - \omega_{\mathbf{0}_e x_e \eta_e})^2}{2\sigma^2_{\eta_e}}} \quad (28)$$

for the broadenings in the imaginary part of the dielectric function, the real part can be obtained analytically from the following Kramers-Kronig transformation:

$$\begin{aligned} \lim_{\Gamma_{\eta_e} \to 0} & \int_{-\infty}^{\infty} \frac{d\omega' G(\omega', \omega_{\mathbf{0}_e x_e \eta_e}, \sigma_{\eta_e})}{\omega_{\mathbf{0}_e x_e \eta_e} - \omega - i\Gamma_{\eta_e}} \quad (29) \\ &= i\pi G(\omega, \omega_{\mathbf{0}_e x_e \eta_e}, \sigma_{\eta_e}) \left[1 - \operatorname{erf}\left(\frac{\omega - \omega_{\mathbf{0}_e x_e \eta_e}}{i\sqrt{2}\sigma_{\eta_e}} \right) \right], \end{aligned}$$

where *erf* is the error function of imaginary argument [41–43]. The influence of the higher-lying transitions is modeled in terms of the dispersive tail of a single effective mode with a transition frequency Ω_q and a static susceptibility q,

$$\chi_b(\omega) = q \frac{\Omega_q^2}{\Omega_q^2 - \omega^2}. \quad (30)$$

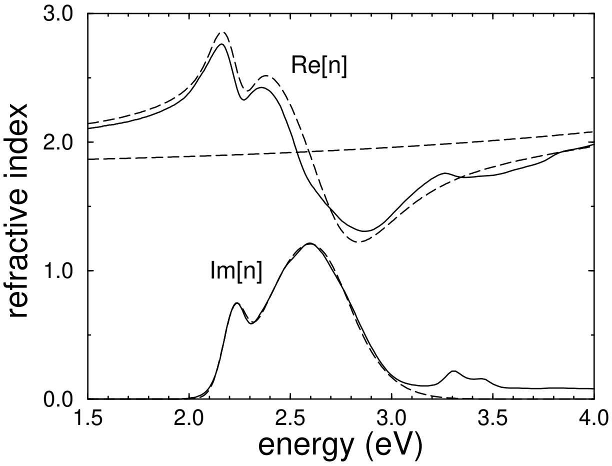

FIG. 4: Real and imaginary part of the refractive index of PTCDA films. Solid: experimental data obtained on PTCDA films deposited on quartz glass [24], dashed: present model calculation at the Γ point of the Brillouin zone for $n_{\|}(\omega) = [\epsilon_{\|}(\omega)]^{1/2}$, and background of the real part of the refractive index, cp. eqs. (26,29,30). Model parameters: $d_0 = 6.45$ Debye, $\hbar\omega_{\text{eff}} = 0.17$ eV, $g^2 = 1.0$, $\nu_{e,max} = 5$, $X(\mathbf{0}_e) = 150$ meV, $V(\mathbf{0}_e) = 47$ meV, $E_{0_g 0_e} + D = 2.180$ eV, $q_b = 2.38$, $\hbar\Omega_b = 7.5$ eV, and $\epsilon^0_{\|} = \frac{1}{2}[\epsilon^0_{xx} + \epsilon^0_{yy}] = 4.07$. For simplicity, the static limits ϵ^0_{xx} and ϵ^0_{yy} are modelled with the same strength q_b of the higher-lying transition. The Gaussian broadening is assumed to increase with the vibronic sublevel η of the exciton eigenstates [25]: For the full width at half maximum, we use 123 meV ($\eta = 0$), 283 meV ($\eta = 1$), 293 meV ($\eta = 2$), 400 meV for ($\eta = 3$), and 433 meV for the higher harmonics.

As the experimental data [24] have been obtained on poly-crystalline samples with a random azimuthal orientation of the unit cell in Fig. 1 in the substrate plane, we have performed an averaging over the two in-plane components of the dielectric tensor, $\epsilon_{\|} = \frac{1}{2}(\epsilon_{xx} + \epsilon_{yy})$, before calculating the complex refractive index $n_{\|} = [\epsilon_{\|}]^{1/2}$. The comparison of this quantity with the experimental data [24] is shown in Fig. 4. For the overall oscillator strength of the HOMO-LUMO transition, we find the best agreement of our calculation with the measured extinction coefficient for a transition dipole of $d_0 = 6.45$ Debye.

Details of the calculated lineshape like the Gaussian broadening parameters were obtained by a mean least squares fit to the measured data [24], excluding the tail beyond 3.2 eV and the observed transition pair at about 3.3 eV and 3.5 eV [25]. As the measured data are not fully Kramers-Kronig consistent, all of our parameters are adjusted to the extinction coefficient $\Im[n_{\|}(\omega)]$. The most important microscopic exciton transfer parameter is the value for the transfer to the stack neighbours. Comparing the fitted value $X(\mathbf{0}_e) = 2W(\mathbf{0}_e) + M(\mathbf{0}_e) = 150$ meV and the asymptotic value $M(\mathbf{0}_e) = -14$ meV for large crystallites, we deduce an interaction among stack neighbours of about $W(\mathbf{0}_e) = 82$ meV, cp. Sec. III. The sharp increase of the broadening σ_{η_e} between $\eta_e = 0$ and

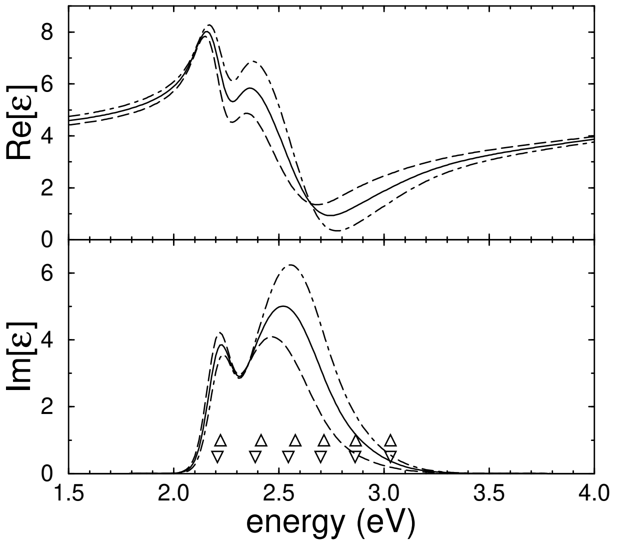

FIG. 5: Calculated diagonal components of the frequency-dependent dielectric tensor, assuming the same background for both directions. Dashed: $\epsilon_{xx}(\omega)$, dash-dotted: $\epsilon_{yy}(\omega)$, solid: average $\epsilon_{\|}(\omega)$, as used for the definition of $n_{\|}(\omega)$ displayed in Fig. 4. The $\triangle$ and $\triangledown$ signs indicate the positions of the upper and lower Davydov components, contributing to $\epsilon_{yy}(\omega)$ and $\epsilon_{xx}(\omega)$, respectively. The model parameters are given in the caption of Fig. 4.

$\eta_e = 1$ cannot be explained by the present model calculation based on the deformation of a single *effective* internal mode. It simulates broadening phenomena beyond the present model, like the elongations of various internal modes in the relaxed excited state of the monomer [27], and the spreading of the deformation cloud around an excited molecule [18].

The calculated extinction coefficient in Fig. 4 is in good qualitative agreement with the data obtained on poly-crystalline films grown on other non-reactive substrates. However, PTCDA films grown on different substrates show a significant scatter of the peak value of the extinction coefficient: For passivated GaAs substrates, it is about 1.0 [44, 45], 1.2 for the films on quartz glass reported in Fig. 4 [24], and 1.4 for growth on passivated Si [44, 45]. Therefore, a determination of the amount of voids in the different thin films and of the average orientation of the molecules would be highly desirable [46]. Using the corresponding measured data for a determination of the size of the optical coupling strength, this scatter of about $\pm 20\%$ in the maximum extinction coefficient would be reflected in changes of $\pm 10\%$ in the HOMO-LUMO transition dipole moment, or $d_0 = 6.45 \pm 0.7$ Debye.

The two different diagonal elements of the frequency-dependent dielectric tensor reported in Fig. 5 are not only different in size because of the trigonometric functions entering the length of $\mathbf{d}_A \pm \mathbf{d}_B$, but the relative ratios depend in a non-trivial way on the vibronic level. Even though the Davydov splitting is quite small, the corresponding oscillator strengths result in a pronounced

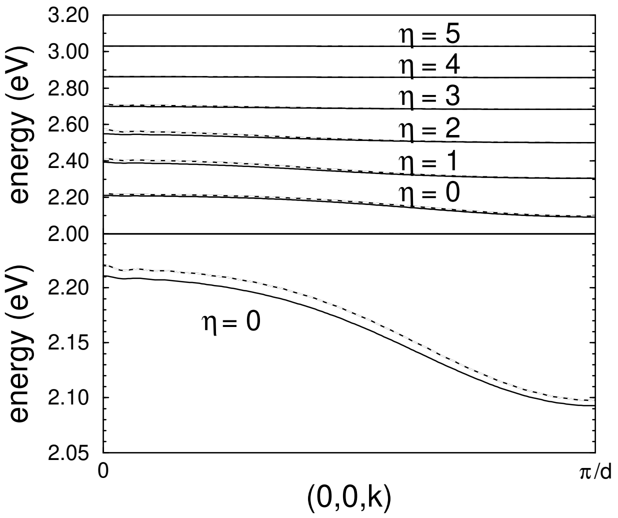

FIG. 6: Dispersion of the Frenkel excitons along $\mathbf{k}_e = (0,0,k_e)$, i.e. in the direction orthogonal to the plane in Fig. 1. Upper: $E_{\mathbf{k}_e x_e \eta_e}$ (solid) and $E_{\mathbf{k}_e y_e \eta_e}$ (dashed), for the vibronic sublevels $\eta_e = 0,1,2,3,4,5$. Lower: dispersion of the lowest vibronic sublevel $E_{\mathbf{k}_e x_e 0_e}$ (solid) and $E_{\mathbf{k}_e y_e 0_e}$ (dashed).

difference between the lineshapes. Qualitatively similar anisotropies of the dielectric tensor were observed in recent ellipsometric investigations of PTCDA crystals [47], revealing small peaks corresponding to the different vibronic sub-bands. In Fig. 5, these structures are not resolved because the fit to the extinction coefficient in Fig. 4 resulted in rather large Gaussian broadenings of the higher harmonics.

V. k-SPACE DISPERSION OF FRENKEL EXCITONS AND DENSITY OF STATES

Using the same microscopic model as in Sec.III, we can compute the exciton transfer energies $M(\mathbf{k}_e)$ and $V(\mathbf{k}_e)$ for any wave vector. Concerning the stack neighbours, the reference value $W(\mathbf{0}_e) = 82$ meV obtained in Sec. IV is generalized to $W(\mathbf{k}) = W(\mathbf{0}_e)\exp(\pm i\mathbf{k}_e\mathbf{a})$, where $\mathbf{a}$ is the lattice vector along the stacking direction of the monoclinic crystal. As exciton transfer to the stack neighbours dominates over the transfer to all other molecules, wave vectors with a large projection on this stacking direction produce a large dispersion, cp. Fig. 6 for the dispersion along wave vectors $(0,0,k_e)$ orthogonal to the plane displayed in Fig. 1.

Compared to the transition energy $E_{0_g 0_e} = 2.18$ eV entering the model calculation, one can distinguish two main contributions to the dispersion of the lowest vibronic sublevel of the Frenkel exciton. First, the energies $E_{\mathbf{k}_e x_e 0_e}$ and $E_{\mathbf{k}_e y_e 0_e}$ are shifted by the diagonal elements of the block-diagonalized Hamiltonian (13), $S^2_{0_g 0_e}(X(\mathbf{k}_e) \mp V(\mathbf{k}_e))$, resulting in a shift upwards at Γ and downwards at the edge of the Brillouin zone by approximately $2S^2_{0_g 0_e} W(\mathbf{0}_e)\cos(k_e d)$. Sec-

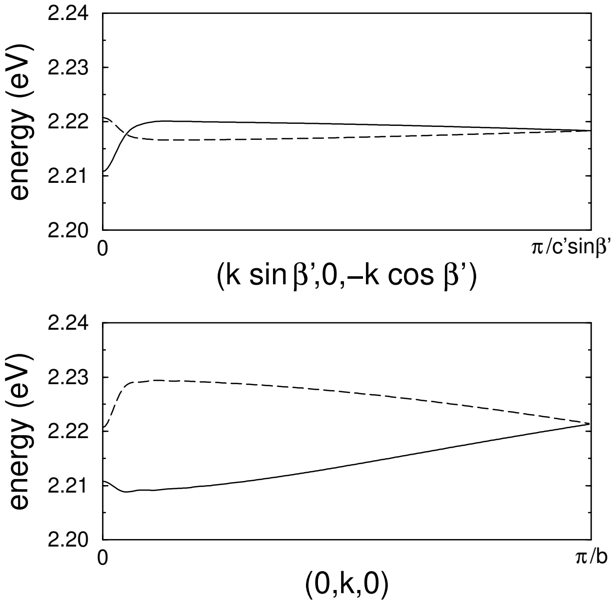

FIG. 7: Dispersion of Frenkel excitons for wave vectors orthogonal to the stack direction $\mathbf{a}$. Upper: lowest vibronic sublevel $E_{\mathbf{k}_e x_e 0_e}$ (solid) and $E_{\mathbf{k}_e y_e 0_e}$ (dashed) for $\mathbf{k}_e = (k\sin\beta', 0, -k\cos\beta')$, lower: same for $\mathbf{k}_e = (0, k, 0)$, where $\beta' = 120.5^0$ is the angle between $\mathbf{a}$ and the lattice vector $\mathbf{c}'$ in Fig. 1.

ond, the lowest vibronic level is pushed down by the interactions with the higher ones, resulting in a shift of $-\sum_{\nu_e\neq 0}(S_{0_g0_e}S_{0_g\nu_e}(X(\mathbf{k}_e)\mp V(\mathbf{k}_e))^2/(\nu_e\hbar\omega_{\rm eff})$ in second order perturbation theory, so that the dominating contribution of the stack neighbours is proportional to $-\cos^2(k_e d)$. As this trigonometric dependence gives the same value at Γ and $k_e = \pi/d$, the energy difference between the surface of the Brillouin zone and Γ is mainly determined by the diagonal first order contribution of the stack neighbours, or $-4S^2_{0_g0_e}W(\mathbf{0}_e) = -121$meV. Higher order perturbations, exciton transfer to more distant equivalent sites and Davydov splitting have a much weaker influence, changing this value by less than 10 meV.

A similar dispersion as in Fig. 6 has been observed recently for the wave vector dependent dielectric function derived from electron energy loss spectroscopy (EELS) on single crystals of α-PTCDA [48]. The calculation of the corresponding excitations requires a generalization of eqs. (22,23) to finite wave vectors, resulting in response functions agreeing qualitatively with the observed lineshapes [49].

For wave vectors orthogonal to the stack direction, the influence of the stack neighbours is excluded, resulting in a much smaller dispersion, cp. Fig. 7 for a plane in reciprocal space passing through Γ. The corresponding dispersion in the plane at the boundary of the Brillouin zone with $\mathbf{k}_e = (k_1\sin\beta', k_2, \pm\pi/d - k_1\cos\beta')$ is qualitatively similar to Fig. 7, but the modulation is somewhat smaller.

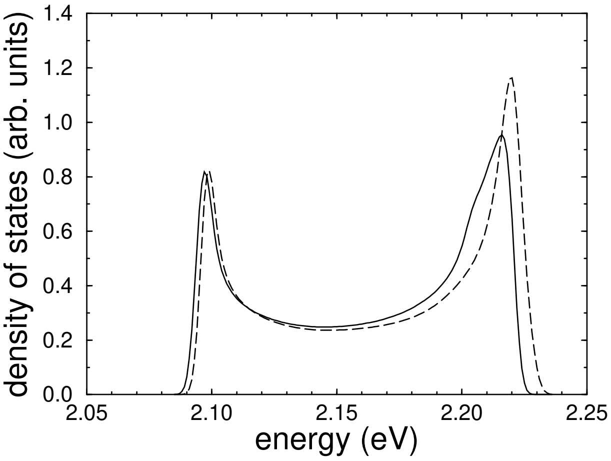

FIG. 8: Density of states on the lowest exciton dispersion branches $E_{\mathbf{k}_e x_e 0_e}$ (solid line) and $E_{\mathbf{k}_e y_e 0_e}$ (dashed), cp. Figs. 6 and 7.

The density of states (DOS) for the lowest branch of the Frenkel exciton dispersion is shown in Fig. 8. It has been calculated over a grid of 10^4 wave vectors including a Gaussian broadening of FWHM = 5 meV. The asymmetry of the DOS is due to the interactions between different vibronic basis states in the Hamiltonian (13) and to matrix elements of exciton transfer beyond the stack neighbours, resulting in deviations of a cosine-like exciton dispersion along the direction in $\mathbf{k}$ space shown in Fig. 6.

Assuming that the Frenkel excitons excited at the Γ point of the Brillouin zone can thermalize via inelastic scattering at intra- and intermolecular phonons into any state on the lowest dispersion branches, the final distribution over the DOS should follow Boltzmann statistics. As two out of three directions in $\mathbf{k}$ space produce a rather flat dispersion, cp. Fig. 7, whereas the third direction in Fig. 6 has a parabolic mimimum, the average thermal energy should be approximately $k_BT/2$ above the dispersion minimum. In Fig. 9, a linear slope of the thermal energy of about $1.1k_BT/2$ is realized between $T = 40$ K and $T = 140$ K. The deviations at lower temperature are related to details of the exciton dispersion in the plane at the surface of the Brillouin zone and to the freezing out of the occupation of the upper dispersion branch $E_{\mathbf{k}_e y_e 0_e}$. At high temperatures, the pronounced non-parabolicity of the exciton dispersion leads to a steeper dependence of the thermal energy.

In the following, the thermalized population of the Frenkel excitons on the dispersion branches $E_{\mathbf{k}_e x_e 0_e}$ and $E_{\mathbf{k}_e y_e 0_e}$ will be discussed as a possible origin of the redshifted photoluminescence of crystalline PTCDA.

VI. PHOTOLUMINESCENCE

A. PL spectra in solution

In solution, the apparent Stokes shift between the lowest absorption band and the highest PL band is about 30 to 40 meV [6, 12], and it was shown before that this energy difference can be assigned to the deformations of the low-frequency internal breathing modes in the relaxed excited state of the molecule [23, 27, 28]. For PTCDA dissolved in DMSO, the PL decays within 4.0 ± 0.5 ns [12]. The corresponding PL rate can be obtained from a generalization of the Einstein coefficient for spontaneous emission [50] to the case of a single effective internal mode,

$$\begin{aligned} \Gamma_{PL} &= \sum_{\nu_g} \Gamma(|0_e\rangle \rightarrow |\nu_g\rangle) \qquad (31) \\ &= \sum_{\nu_g} \frac{d_0^2 P_{\nu_g}(g^2)}{3\pi\epsilon_0 \hbar c^3} \omega^3_{\nu_g 0_e} n^3(\omega_{\nu_g 0_e}), \end{aligned}$$

where $P_{\nu_g}(g^2)$ can be calculated in analogy to eq. (1), and $n(\omega_{\nu_g 0_e})$ is the refractive index of the solvent for the transition frequency between the lowest vibronic level 0_e in the excited electronic state and the vibronic level ν_g in the electronic ground state. Based on a reference energy of $\hbar\omega_{0_g 0_e} = 2.32$ eV for the highest PL band observed [12], an effective vibrational mode of 0.17 eV, an argument of $g^2 = 0.76$ in the Poisson progression as derived from a calculation of the absorption lineshape of PTCDA dissolved in DMSO [27], and the refractive index of DMSO in the visible of $n = 1.417$ [51], the observed lifetime of $\tau_{PL} = 1/\Gamma_{PL} = 4.0 \pm 0.5$ ns [12] can be used for an estimate of $d_0 = 7.06 \pm 0.43$ Debye for the molecular transition dipole, in the same range as the value 7.4 ± 0.7 Debye deduced from absorption measurements of dissolved PTCDA [16] and the value of 6.45 ± 0.7 Debye obtained from the analysis of thin film absorption in Sec. IV.

B. PL of PTCDA thin films and single crystals

At low temperature, the time-dependence of the photoluminescence (PL) spectra of α-PTCDA single crystals is dominated by two radiative decay channels with lifetimes of about 13 and 33 ns, each consisting of a main peak around 1.82 eV and a smaller low-energy satellite around 1.67 eV [21]. Furthermore, the data contain a high-energy satellite around 1.95 eV, in agreement with earlier stationary PL studies [7]. With respect to the lowest absorption maximum around 2.23 eV, the largest vibronic subband of the low-temperature PL shows a Stokes shift of about 0.41 eV.

The PL spectra at room temperature are more controversial, showing a maximum around 1.70 eV [12] or 1.80 eV [52], probably depending on details of the film preparation. From time-resolved measurements, there is some

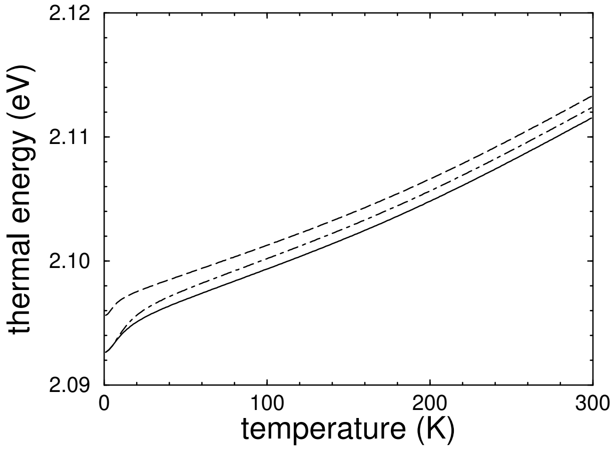

FIG. 9: Average thermal energy of the excitons on the lowest dispersion branch according to Boltzmann statistics: Frenkel exciton population on the dispersion relation $E_{\mathbf{k}_e x_e 0_e}$ (solid line), $E_{\mathbf{k}_e y_e 0_e}$ (dashed), and thermal average (dash-dotted), where the occupation of the upper branch $E_{\mathbf{k}_e y_e 0_e}$ freezes out for $T \rightarrow 0$.

evidence for a shift from a peak position of about 1.80 eV at early times ($<$ 50 ps) towards 1.76 eV for longer delay times ($>$ 5 ns) and time-integrated spectra [53]. In subsequent time-resolved PL studies of single crystals of α-PTCDA in the temperature range $T = 10$ K to 300 K, the PL spectra were resolved into different contributions with decay times ranging from 3 to 50 ns, and the PL channel decaying with a radiative lifetime of $\tau_{\rm rad} = 13$ ns at low-temperature is quenched above about $T = 200$ K due to activated non-radiative decay [20, 22]. In the following, it will be shown that this PL band can be assigned to vertical recombination starting from the indirect minimum of the Frenkel exciton dispersion discussed in Sec. V.

C. Thermalization scenario

As a scenario for the relaxation of the optical excitation and PL at low temperature, we propose the scheme displayed in Fig. 10. The absorption at Γ starts in the lowest vibronic level of the electronic ground state and results in a Frenkel exciton with vanishing wave vector. Subsequent emission processes involving vibronic excitations of suitable energy and wave vector result eventually in exciton states around the minimum of the lowest dispersion branch.

These thermalization processes should be relatively fast as the lifetime of the corresponding high-frequency vibrational modes is of the order of few picoseconds, an estimate which can be deduced both from the linewidth in resonant Raman spectra [27] and dephasing times observed in pump-probe spectra on a similar thin film material (Me-PTCDI), where the A_g modes appeared as damped oscillations in real time [54]. The thermaliza-

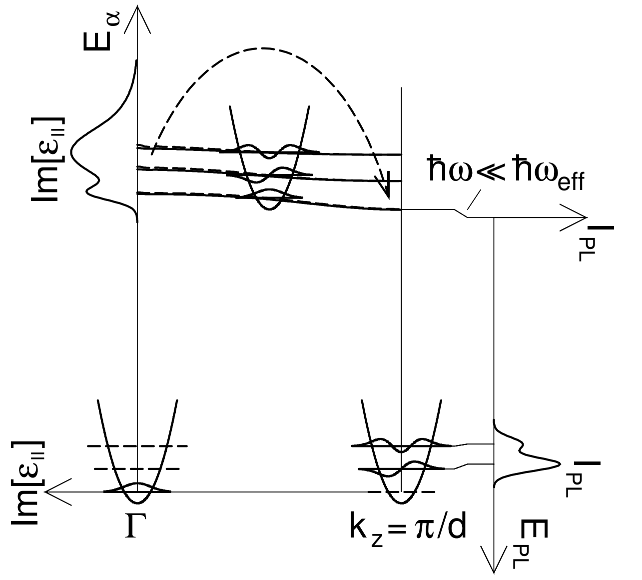

FIG. 10: Schematic model of the optical excitation and recombination cycle in crystalline PTCDA at low temperature. After photon absorption at Γ, subsequent scattering processes (dashed arrow) towards the dispersion minimum at the surface of the Brillouin zone result in a thermalized distribution of excitons around the minimum of the lowest branch of the Frenkel exciton dispersion. A further red-shift of the PL is due to a lowering of this relaxed excited state by contributions of low-frequency internal breathing modes and external phonons far below the effective internal mode (shift downwards of the reference for the PL energy) and correlations between the vibronic sublevels after recombination (shift upwards of the energy of the final states after PL). The lineshape observed in optical absorption is visualized as $\Im[\epsilon_{||}]$ as a function of the energy E_α measured with respect to the ground state at Γ, while the origin of the PL energy scale E_{PL} is related to the lowest relaxed excited state available. For the exciton dispersion branches, their relation to the vibronic levels of an excited molecule is visualized for $k_z = \frac{\pi}{2d}$ where the dominating influence of the stack neighbours on the dispersion vanishes. Vibronic levels ν_g not involved in the absorption and PL transitions are visualized as dashed lines.

tion of the lowest internal vibrations and the external phonons should be somewhat slower because they are excited to rather high vibronic levels and, as a tendency, show slower dephasing [54] and therefore longer lifetimes. Nevertheless, this thermalization scenario should be accomplished after a few tens of picoseconds, i.e. within the resolution in recent time-resolved PL measurements [21].

The low-lying excitonic eigenstates around the dispersion minimum are obvious candidates for a red-shifted PL transition towards the electronic ground state. In order to distinguish these eigenstates from the corresponding set of vibronic basis states related to eqs. (14,15), the excitonic eigenstates $|\mathbf{k}_e\gamma_e, \eta_e = 0_e\rangle$ on the lowest dispersion branch will be abbreviated as $|\mathbf{k}_e\gamma_e\tilde{0}_e\rangle$ in the following.

D. Final states after vertical recombination

As the electronic and vibronic ground state $|g\rangle$ according to eq. (2) has vanishing total momentum, it is not available as a final state after vertical radiative recombination starting from the lowest exciton branch at a different initial wave vector. Therefore, the lowest accessible final states after recombination are vibronic excitations propagating with the same wave vector as the Frenkel exciton before recombination, excluding the vibronic ground state. These states with energy $\nu_g\hbar\omega_{\rm eff}$ can be constructed as Bloch waves based on excited vibronic levels of the molecules in different unit cells:

$$|\mathbf{k}_g\alpha\nu_g\rangle = \frac{1}{\sqrt{N}}\sum_n e^{-i\mathbf{k}_g\cdot\mathbf{R}_{\mathbf{n}\alpha}}|\mathbf{n}\alpha\nu_g\rangle, \tag{32}$$

where the r.h.s. is a shorthand notation for a product state where the molecule α in unit cell $\mathbf{n}$ is in the vibronic state ν_g, while all other molecules are in their vibronic ground states. As discussed in Sec. II for the optical excitation Frenkel excitons, it is useful to perform a rotation from the basis molecules A and B in the unit cell to linear superpositions,

$$\begin{aligned} |\mathbf{k}_g x_g\nu_g\rangle &= \frac{1}{\sqrt{2}}(|\mathbf{k}_g A\nu_g\rangle - |\mathbf{k}_g B\nu_g\rangle) \\ |\mathbf{k}_g y_g\nu_g\rangle &= \frac{1}{\sqrt{2}}(|\mathbf{k}_g A\nu_g\rangle + |\mathbf{k}_g B\nu_g\rangle) \end{aligned} \tag{33}$$

which can be indexed again with the cartesian directions x and y in Fig. 1. Contrary to absorption, we have now two distinct initial states $|\mathbf{k}_e x_e\tilde{0}_e\rangle$ and $|\mathbf{k}_e y_e\tilde{0}_e\rangle$ resulting from the excitations (16) out of the vibronic ground state at Γ, or from thermalization of optically excited Frenkel excitons which were created at the Γ point as $|\mathbf{0}_e x_e\tilde{\eta}_e\rangle$ and $|\mathbf{0}_e y_e\tilde{\eta}_e\rangle$.

E. Model Hamiltonian

In analogy to eq. (8), we can now define a Hamiltonian for the final states after radiative de-excitation:

$$\begin{aligned} H^g(\mathbf{k}_e,\mathbf{k}_g) &= \sum_{\gamma_e\gamma_g}\sum_{\nu_g\neq 0}\left(\nu_g\hbar\omega_{\rm eff} - E_{\mathbf{k}_e\gamma_e\tilde{0}_e}\right) \\ &\times\; b_{\mathbf{k}_e\gamma_e\tilde{0}_e,\mathbf{k}_g\gamma_g\nu_g} b^+_{\mathbf{k}_e\gamma_e\tilde{0}_e,\mathbf{k}_g\gamma_g\nu_g} \\ &+ \sum_{\gamma_e\gamma_g}\sum_{\nu_g\neq 0}\sum_{\mu_g\neq 0} t_{\gamma_e\tilde{0}_e,\gamma_g,\nu_g\mu_g}(\mathbf{k}_e,\mathbf{k}_g) \\ &\times\; b_{\mathbf{k}_e\gamma_e\tilde{0}_e,\mathbf{k}_g\gamma_g\nu_g} b^+_{\mathbf{k}_e\gamma_e\tilde{0}_e,\mathbf{k}_g\gamma_g\mu_g}, \end{aligned} \tag{34}$$

where both γ_e and γ_g are summed over the values x or y. The operators $b_{\mathbf{k}_e\gamma_e\tilde{0}_e,\mathbf{k}_g\gamma_g\nu_g}$ describe a de-excitation process starting from the exciton state $|\mathbf{k}_e\gamma_e\tilde{0}_e\rangle$ on the lowest dispersion branch and ending in an excited vibronic level $|\mathbf{k}_g\gamma_g\nu_g\rangle$ in the electronic ground state, cp. eq. (33). The transfer matrix elements $t_{\gamma_e\tilde{0}_e,\gamma_g,\nu_g\mu_g}(\mathbf{k}_e,\mathbf{k}_g)$ can be obtained without additional assumptions from the quantities used in the calculation of the linear optical properties and the exciton dispersion,

$$\begin{aligned} t_{\gamma_e\tilde{0}_e,\gamma_g,\nu_g\mu_g}(\mathbf{k}_e,\mathbf{k}_g) &= T_{\gamma_e\gamma_g}(\mathbf{k}_e-\mathbf{k}_g) \\ &\times\; S_{\nu_g,\gamma_e\tilde{0}_e}(\mathbf{k}_e)S_{\mu_g,\gamma_e\tilde{0}_e}(\mathbf{k}_e), \end{aligned} \tag{35}$$

where the overlap factors take into account that the exciton eigenstates $\tilde{0}_e$ on the lowest dispersion branch arise from the vibronic sublevels of the excited molecular state by the unitary transformation (16),

$$S_{\nu_g,\gamma_e\tilde{0}_e}(\mathbf{k}_e) = \sum_{\nu_e} u_{\nu_e,\gamma_e\tilde{0}_e}(\mathbf{k}_e)S_{\nu_g\nu_e}. \tag{36}$$

where the vibronic overlaps $S_{\nu_g\nu_e}$ can be calulated from Laguerre's polynomials

$$S_{\nu_g\nu_e} = e^{-g^2/2}g^{\nu_e-\nu_g}\sqrt{\frac{\nu_g!}{\nu_e!}}L_{\nu_g}^{\nu_e-\nu_g}(g^2)$$

for $\nu_g \le \nu_e$, and similarly in the opposite case. Due to the small wave vector of the PL photon, the initial and final wave vectors coincide, so that the transfer matrix elements $T_{\gamma_e\gamma_g}(\mathbf{k}_e-\mathbf{k}_g) = T_{\gamma_e\gamma_g}(\mathbf{0})$ in eq. (35) can be calculated at the Γ point:

$$T_{xx}(\mathbf{0}) = T_{yy}(\mathbf{0}) = \frac{X(\mathbf{0})+V(\mathbf{0})}{2}, \tag{37}$$

$$T_{xy}(\mathbf{0}) = T_{yx}(\mathbf{0}) = \frac{X(\mathbf{0})-V(\mathbf{0})}{2}, \tag{38}$$

with the material parameters $X(\mathbf{0}) = 150$ meV and $V(\mathbf{0}) = 47$ meV, cp. the caption of Fig. 4. The Hamiltonian (34) is block-diagonal with respect to the index pair (γ_e,γ_g), so that the states on each exciton branch γ_e have two independent decay routes, $\gamma_e \to x_g$ and $\gamma_e \to y_g$.

By diagonalizing the Hamiltonian (34) for $\mathbf{k}_g = \mathbf{k}_e$, the final states (33) become correlated through the transfer matrix elements (35). The corresponding unitary transformation from the basis set (33) to the eigenstates $|\mathbf{k}_e,\gamma_g \leftarrow \gamma_e,\eta_g\rangle$ after recombination starting on the exciton branch γ_e can be written in a similar way as eq. (16):

$$|\mathbf{k_e},\gamma_g \leftarrow \gamma_e,\eta_g\rangle = \sum_{\nu_g\neq 0} u_{\nu_g,\gamma_g\leftarrow\gamma_e,\eta_g}(\mathbf{k}_e)|\mathbf{k}_e\gamma_g\nu_g\rangle \tag{39}$$

where the coefficients are again found by a numerical diagonalization.

F. Sum rule for PL coupling strength

The PL transitions towards the vibronic levels $\nu_g \neq 0$ involved in the definition of the Hamiltonian (34) cary transition dipole moments of

$$\langle\mathbf{k}_e\gamma_g\nu_g|e\mathbf{r}|\mathbf{k}_e\gamma_e\tilde{0}_e\rangle = \frac{1}{\sqrt{2}}(\mathbf{d}_A \pm \mathbf{d}_B)S_{\nu_g,\gamma_e\tilde{0}_e}(\mathbf{k}_e), \tag{40}$$

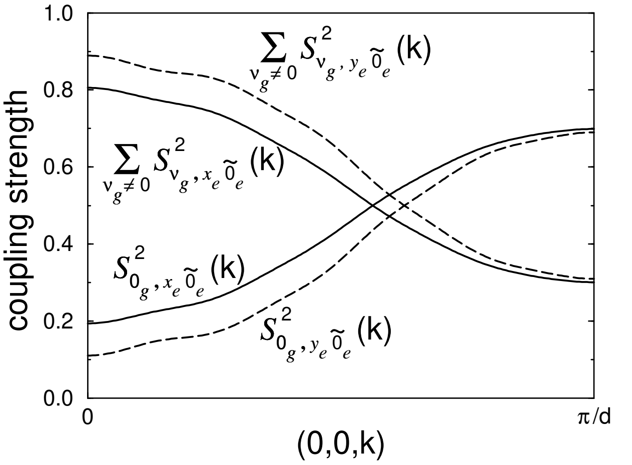

FIG. 11: Coupling strength for excitation from the ground state of the molecular crystal onto the lowest exciton branch, $S^2_{0_g,\gamma_e\tilde{0}_e}(\mathbf{k}_e)$, for $\gamma_e = x_e$ (solid line) and for $\gamma_e = x_e$ (dashed line), as annoted, and the sums $\sum_{\nu_g\neq 0} S^2_{\nu_g,\gamma_e\tilde{0}_e}(\mathbf{k}_e)$ determining the amount of vibronic overlap available for radiative recombination.

where a dipole orientation $(\mathbf{d}_A+\mathbf{d}_B) \parallel \mathbf{e}_y$ applies to $\gamma_e = \gamma_g$, whereas transitions with $\gamma_e \neq \gamma_g$ have dipole moments along $(\mathbf{d}_A-\mathbf{d}_B) \parallel \mathbf{e}_x$.

As the lowest vibronic level $\nu_g = 0$ cannot be reached by vertical PL transitions starting from thermalized excitons around the dispersion minimum, the transition dipole moment available for radiative recombination is below the molecular reference value, as can be deduced from simple completeness arguments. The overlaps $S_{\nu_g,\gamma_e\tilde{0}_e}(\mathbf{k}_e)$ in eqs. (36,40) would allow a complete representation of the vibronic part of the state $|\mathbf{k}_e\gamma_e\tilde{0}_e\rangle$ if the complete basis set $\{|\nu_g\rangle\}$ would be included. However, as $|0_g\rangle$ cannot be reached by the vertical PL transitions, the dipolar coupling strength available in eq. (40) is reduced,

$$\sum_{\nu_g\neq 0} S^2_{\nu_g,\gamma_e\tilde{0}_e}(\mathbf{k}_e) = 1 - S^2_{0_g,\gamma_e\tilde{0}_e}(\mathbf{k}_e), \tag{41}$$

cp. Fig. 11. For the optical absorption at Γ, the exciton transfer reduces the coupling between the lowest vibronic states $S^2_{0_g,\gamma_e\tilde{0}_e}(\mathbf{0}_e)$ with respect to the expected value of $S^2_{0_g0_e}\exp(-g^2) = 0.37$, shifting the transition dipole moments to the higher vibronic levels $\eta_e > 0$. At the boundary of the Brillouin zone, $S^2_{0_g,\gamma_e\tilde{0}_e}(\mathbf{k}_e)$ is increased to about 0.7, so that the complement $1 - S^2_{0_g,\gamma_e\tilde{0}_e}(\mathbf{k}_e)$ is reduced to a value of about 0.3. Therefore, the sum over the squares of the transition dipole moments in eq. (40) is reduced by the same amount, resulting in a slower radiative decay than in the case of a dissolved molecule.

PL channel	η_g	$E^{PL}_{\eta_g}$ (eV)	$(d^{PL}_{\eta_g}/d_0)^2$ (1)	decay rate ($1/\mu s$)	decay time (ns)
$x_e \to x_g$	1	1.816	0.120	34.2	
	2	1.661	0.046	9.3	
	3	1.496	0.010	1.5	
	all		0.177	45.2	22.1
$x_e \to y_g$	1	1.826	0.087	25.1	
	2	1.664	0.028	5.8	
	3	1.497	0.006	0.9	
	all		0.121	31.9	31.3
$y_e \to x_g$	1	1.830	0.088	25.8	
	2	1.668	0.029	6.1	
	3	1.500	0.007	1.0	
	all		0.126	33.0	30.3
$y_e \to y_g$	1	1.820	0.122	35.0	
	2	1.664	0.048	9.9	
	3	1.499	0.011	1.6	
	all		0.184	46.7	21.4
$x_e \to (x_g, y_g)$	all		0.299	77.1	13.0
$y_e \to (x_g, y_g)$	all		0.310	79.7	12.6

TABLE I: Radiative recombination rates according to eq. (43), for initial states at the minimum of the exciton dispersion in Fig. 6, $\mathbf{k}_e = (0, 0, \pi/d)$. In the calculated rates, a shift to lower energies by 85 meV has been included, cp. eq. (44), related to the Stokes shift arising from low-frequency internal and external vibrations.

G. PL lineshape

The transition dipoles for PL towards the final states (39) can be obtained by applying the same unitary transformation to the transition dipoles in eq. (40):

$$\begin{aligned}\mathbf{d}_{\mathbf{k}_e,\gamma_g\leftarrow\gamma_e,\eta_g;\mathbf{k}_e\gamma_e\tilde{0}_e} &= \langle \mathbf{k}_e, \gamma_g \leftarrow \gamma_e, \eta_g | e\mathbf{r} | \mathbf{k}_e \gamma_e \tilde{0}_e \rangle \qquad (42)\\ &= \frac{1}{\sqrt{2}}(\mathbf{d}_A \pm \mathbf{d}_B)\\ &\times \sum_{\nu_g \neq 0} u_{\nu_g,\gamma_g\leftarrow\gamma_e,\eta_g}(\mathbf{k}_e) S_{\nu_g,\gamma_e\tilde{0}_e}(\mathbf{k}_e),\end{aligned}$$

with a dipole orientation along y in Fig. 1 for $\gamma_e = \gamma_g$, and along x for $\gamma_e \neq \gamma_g$.

The exciton dispersion in Fig. 6, the density of states in Fig. 8 and the thermal energy in Fig. 9 exclude any energetic contributions of low-frequency modes far below the effective internal mode included in the present Frenkel exciton model. From a quantitative analysis of the corresponding resonant Raman spectra [27, 55], the reorganization energies related to low-lying internal vibrations and to external phonon modes were estimated to be about 14 meV and 41 meV, respectively [23], resulting in a Stokes shift of 110 meV.

Applying this shift downwards to the positions of the PL channels obtained from a diagonalization of the Hamiltonian (34), the resulting energies turn out to be about 25 meV below the measured values [21]. In order to make the calculated positions coincide with the measured position of 1.82 eV for the largest PL subband [21], we use a reduced Stokes shift arising from the low-frequency vibrations of only 85 meV instead of 110 meV. Even though this change of 25 meV might seem small with respect to the total Stokes shift of 0.41 eV between the lowest absorption subband and the highest PL subband, the need to reduce the contribution of the low-frequency vibronic modes to the Stokes shift indicates limitations of the effective mode model applied in the present work.

The recombination rates into the various final states are calculated from the following generalization of eq. (32):

$$\begin{aligned}\Gamma^{PL}_{\gamma_g\leftarrow\gamma_e} &= \sum_{\eta_g} \Gamma_{\mathbf{k}_e,\gamma_g\leftarrow\gamma_e,\eta_g;\mathbf{k}_e\gamma_e\tilde{0}_e} \qquad (43)\\ &= \sum_{\eta_g} \frac{\mathbf{d}^2_{\mathbf{k}_e,\gamma_g\leftarrow\gamma_e,\eta_g;\mathbf{k}_e\gamma_e\tilde{0}_e}}{3\pi\epsilon_0\hbar c^3}\omega^3 n_x(\omega) n_y(\omega) n_z(\omega),\end{aligned}$$

where

$$\omega = \omega_{\mathbf{k}_e,\gamma_g\leftarrow\gamma_e,\eta_g;\mathbf{k}_e\gamma_e\tilde{0}_e} - 85 \text{ meV} \qquad (44)$$

is an abbreviation for the PL transition frequency resulting from the diagonalization of the Hamiltonian (34), shifted by the Stokes shift assigned to the low-frequency vibrational modes. The frequency-dependence of the refractive indices n_x and n_y is calculated from the anisotropic diagonal elements ϵ_{xx} and ϵ_{yy} of the dielectric tensor shown in Fig. 5, whereas $n_z = \sqrt{1.85}$ [38] is assumed to be frequency-independent. The distribution of the radiative recombination rates over the final states (39) is given in Table I.

In the temperature range of about $T = 10$ K investigated in recent time-resolved PL studies, the radiative lifetime of the dominating PL channel was found to be 12.7 ± 0.4 ns. From the thermal averages in Fig. 9, it is obvious that the exciton population on the upper dispersion is irrelevant in this temperature regime, restricting recombination to initial states on the lower dispersion branch x_e. Both the wave vector $\mathbf{k}_e = (0, 0, \pi/d)$ used for the calculation of the recombination rates in Table I and the thermal average at $T = 10$ K in Fig. 9 are about 1.5 meV above the dispersion minimum, so that the (tiny) influence of this small energetic shift on the recombination rates is similar. Therefore, the values tabulated in Table I are suitable for a comparison with the experimental findings, and the calculated radiative lifetime of 13.0 ns coincides with the measured value of 12.7 ± 0.4 ns within the experimental uncertainty.

In the measured lineshape of this PL channel shown in Fig. 12, each vibronic subband is considerably broadened and shows a large asymmetry. The calculated PL spectra are based on the rates in Table I and two different models for the asymmetric shape of each subband.

In the first model, the elongations of the 6 external phonon modes and the 3 lowest internal breathing modes

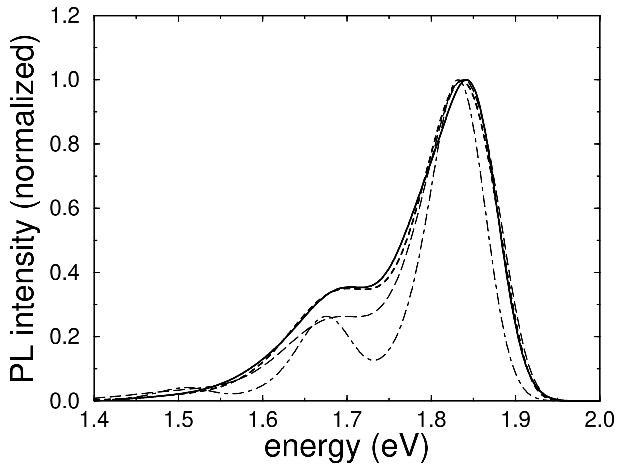

FIG. 12: Comparison of the measured PL band decaying within 12.7 ± 0.4 ns at $T = 11$ K [21] and the calculated PL lineshape. Solid line: fit of the measured spectra [21], short dashes: model lineshape based on subbands calculated from a Poisson distribution of an effective low-frequency mode of 30 meV with $g^2 = 2.0$ and increasing Gaussian broadenings for the higher harmonics at lower photon energy, dot-dashed line: calculated from the radiative recombination rates in Table I and a product of the Poisson distributions of the 6 external phonon modes and the 3 lowest internal A_g vibrations, with arguments derived from resonant Raman spectra [23], long dashes: calculated with the rates in Table I and the same Poisson distribution for an effective low-frequency mode as for the short-dashed line. All the PL spectra shown are normalized to the same maximum value.

are included explicitly, and their elongations are estimated from their respective resonant Raman spectra [23]. The resulting asymmetric subbands are centered at the energetic positions taken from Table I, including a Gaussian broadening of FWHM = 60 meV in order to make the upper edge coincide with the measured shape. The multiplication with the factor $\omega^3 n_x n_y n_z$ related to the density of state of the PL photons was performed after introducing the broadened subbands. Even though the same elongations of these 9 low-frequency modes result in quantitative agreement with the broadening required for the lowest absorption subband [23], two shortcomings of this PL model lineshape are obvious: First, the asymmetry of each subband is underestimated with respect to the measured spectra, and second, the origin of the required Gaussian broadening is unclear. This demonstrates that the replacement of the high-frequency internal modes by an effective high frequency mode in the present Frenkel exciton model and the subsequent inclusion of the missing low-frequency vibrations in the shape of the vibronic subbands of the effective mode does not provide a quantitative understanding of the asymmetry and broadening of the subbands. Alternatively, the elongations of the low-frequency internal modes in the relaxed excited state could be somewhat larger than the values calculated for the free molecule [27]. In principle, these elongations can be deduced from the laser induced fluorescence spectra measured on single PTCDA molecules in He nanodroplets [34], so that the validity of the approach used in the calculation could be tested.

The second model is based on an assignment of the observed assymmetry to a single Poisson distribution of an effective low-frequency mode of 30 meV with $g^2 = 2.0$. Together with suitable Gaussian broadenings, such asymmetric broadened shapes for the different vibronic subbands account quite well for the measured spectra, cp. Fig. 12. Using these shapes for a broadening of the transition energies in Table I, the calculated model lineshape is in much better agreement with the measured spectra. However, the relative intensity of the calculated subband around 1.66 eV is somewhat underestimated with respect to the dominating transition around 1.82 eV and the second sideband around 1.50 eV.

The energetic position of the observed Frenkel exciton PL shows a linear shift of 4.8×10^{-2} meV/K with rising temperature [22], coinciding within the experimental error margin with the slope of the average thermal energy reported in Fig. 9.

VII. DISCUSSION

Contrary to previous models of the optical properties of PTCDA based on both Frenkel and charge transfer excitons [18, 19], the present investigation has focused on the role of the Frenkel excitons alone. Excluding the fact that the broadenings of different vibronic subbands have been adjusted to the observed spectra, this approach requires only six microscopic parameters for the calculation of the optical absorption, including four related to molecular quantities: The molecular transition energy $E_{0_g 0_e}$, red-shifted by the crystalline surroundings, the HOMO-LUMO transition dipole d_0, an effective internal vibration $\hbar\omega_{\text{eff}}$, and the elongation of this mode, $g^2 = \lambda/(\hbar\omega_{\text{eff}})$. The two additional parameters in the crystalline phase are two matrix elements for the transfer of the Frenkel excitons, called $T_{AA}(\mathbf{0}) = X(\mathbf{0})$ and $T_{AB}(\mathbf{0}) = V(\mathbf{0})$.

The most uncertain of these parameters is the molecular transition dipole. As discussed above, the transition dipole of $d_0 = 6.45 \pm 0.7$ Debye derived from the measured extinction coefficient [24] displayed in Fig. 4 and similar data [44, 45] is at the lower edge of the value of 7.4 ± 0.7 Debye deduced from the absorption of dissolved PTCDA [16] and the value of $d_0 = 7.06 \pm 0.43$ Debye obtained from the PL decay of PTCDA dissolved in DMSO [12], cp. Secs. IV and VI A, so that an error margin of 15% seems to be realistic. From the excellent agreement of the radiative recombination rate calculated in Sec. VI with the measured PL decay, our rather low value for the molecular transition dipole seems to be corroborated. However, this calculation of the PL recombination rate was based on a strong reduction of the sum over the squared dipole moments involved, cp. the discussion of Fig. 11. Therefore, the agreement between the calculated and measured decay time of the PL cannot be used for a confirmation of the rather low transition dipole moment without a discussion of the influence of the other microscopic parameters.

The effective vibronic mode of $\hbar\omega_{\rm eff} = 0.17$ eV can be related quantitatively to an average of the most prominent internal breathing modes observed in resonant Raman spectra, so that its uncertainty is in the range of 1%. The value of $g^2 = 1.0$ for the argument of the Poisson progression determining the Franck-Condon factors is somewhat below the value calculated from the relaxed geometry of a free PTCDA molecule [27], but a range of $g^2 = 1.0 \pm 0.1$ seems to be realistic. Finally, the fourth molecular parameter, i.e. the transition energy $E_{0_g 0_e} = 2.18$ eV, is determined from the energetic position of the experimental absorption lineshape or from the extinction coefficient, so that its error margin is negligible.

Concerning the matrix elements for the transfer of Frenkel excitons, they depend on the square of the transition dipole moment, so that formally an uncertainty of 30% can be expected from the broad range of acceptable transition dipoles. However, in Sec. III it was shown that the exciton transfer towards the same basis molecule in different unit cells is dominated by the transfer to the stack neighbours, whereas the transfer between the two different basis molecules $A \leftrightarrow B$ involves mainly the twelve nearest neighbours. Precisely for these matrix elements, only a range of acceptable values could be deduced from two different screening models for the interactions between the distribution of transition charges. As the sums over the transfer matrix elements, $X(\mathbf{0})$ and $V(\mathbf{0})$, were determined from a comparison with the measured extinction coefficient, the uncertainty of the transition dipole moment would merely change the acceptable range for realistic transfer matrix elements, whereas their values would hardly change. Therefore, the matrix elements for exciton transfer to these molecules in the immediate surroundings should have an uncertainty far below the 30% one could expect from the range of possible transition dipole moments.

Both the exciton transfer matrix elements and the argument of the vibronic progression influence on the second moment of the absorption lineshape and the distribution of oscillator strengths over subsequent vibronic levels, so that they depend critically on each other. Considering a reduced value of $g^2 = 0.9$, a shape of $\Im[\epsilon_{||}]$ similar to Fig. 5 requires an increase of the matrix elements for exciton transfer by 10%, $X(\mathbf{0}) = 0.165$ eV and $V(\mathbf{0}) = 0.052$ eV, and the resulting fit of the extinction coefficient in Fig. 4 would be slightly worse but still acceptable. However, an enlarged exciton transfer results in a stronger reduction of the dipolar coupling strength available for radiative recombination from the minimum of the exciton dispersion with respect to Fig. 11, so that the radiative lifetime would increase to 15.9 ns. The corresponding recombination rate would therefore be below the observed value, a deficiency which could be cured by increasing the transition dipole to about $d_0 = 7.15$ Debye. Even though this value is still within the range discussed in the literature and in the analysis of different experimental data sets performed in the present work, it would no more allow to model the experimental extinction coefficient shown in Fig. 4. As a 20% higher extinction coefficient was found in different thin film samples [45], this is not necessarily a shortcoming, as the films used in Ref. [24] could have had a volume filling factor significantly below one. From this discussion of the inter-dependence of the different model ingredients we conclude that a more precise knowledge of the material parameters needed would most of all require experimental reference data where both the average orientation of the crystallites and the volume filling factor are known.

A question going beyond the approach suggested in the present work is why the influence of CT excitons can be ignored at all. The fact that a pure Frenkel exciton approach with carefully derived microscopic transfer parameters can be used for a quantitative model of both the linear optical properties and the photoluminescence suggests two possibilities: First, the position of the most important CT states could coincide so well with one of the calculated vibronic subbands in linear absorption that its mixing with the Frenkel exciton has only a weak influence on the lineshape, and second, the matrix element for this mixing could be lower than the values assumed in previous model calculations [18, 19], e.g. due to compensations between the matrix elements for electron and hole transfer.

The good agreement of the pure Frenkel exciton model with the low-temperature PL spectra is a further indication that the Frenkel-CT mixing is weak. A previous assignment of three much slower PL decay rates to anion-cation pairs and excimers [20, 23] underlines the fact that the transition dipole moments of the CT states are small, in agreement with three independent microscopic calculations [16, 19, 23]. If the mixing between CT and Frenkel excitons would be strong, the slower PL channels could borrow a sizeable fraction of the transition dipoles involved in the PL channel calculated in the present work, so that their long radiative lifetimes would speed up and the PL from Frenkel excitons would slow down. The completely different temperature-dependent quenching of the various PL channels [20–22] is a further indication that PL from Frenkel and CT states involves rather different relaxed excited states.

The matrix elements for electron and hole transfer result in a wave vector dependence of the mixing between Frenkel and CT excitons [16]. If the transfer parameters for both types of charge carriers are equal [15], they interfere constructively at the Γ point and destructively at the surface of the Brillouin zone, so that Frenkel and CT states decouple for PL from the minimum of the Frenkel exciton dispersion. On the other hand, three calculations of these transfer parameters with different quantum chemical techniques agree on the fact that electron transfer between stack neighbours is somewhat larger than the corresponding hole transfer [16, 19, 23]. In this case, the mixing between Frenkel and CT states would be dominated by electron transfer throughout the Brillouin zone, with a small wave vector dependent modulation resulting from hole transfer. As long as the size of the electron and hole transfer is still open to debate, a definitive assessment of the size of the mixing between Frenkel and CT states will require further microscopic calculations of the corresponding matrix elements for electron and hole transfer, and an application of models combining Frenkel and CT excitons [18, 19] to PL would be helpful.

Finally, a microscopic understanding of the chemical trends between different perylene derivatives like PTCDA and MePTCDI would be desirable, and the availability of time-resolved PL data over a large temperature range for similar substances like MePTCDI single crystals could help to elucidate the complicated photophysics of this important class of organic semiconductors.

Acknowledgements We thank A. Yu. Kobitski for sharing unpublished PL data. Financial support by the DFG is gratefully acknowledged.

[1] H. Neureiter, W. Gebauer, C. Väterlein, M. Sokolowski, P. Bäuerle, and E. Umbach, Synth. Met. **67**, 173 (1994).
[2] J. Simon, and J. -J. André, *Molecular Semiconductors*, Springer (Berlin 1985).
[3] R. Hajlaoui, G. Horowitz, F. Garnier, A. Arce-Brouchet, L. Laigre, A. El Kassimi, F. Demanze, and K. Kouki, Adv. Mater. **9**, 389 (1997).
[4] S. R. Forrest, Chem. Rev. **97**, 1793 (1997).
[5] A. J. Lovinger, S. R. Forrest, M. L. Kaplan, P. H. Schmidt, and T. Venkatesan, J. Appl. Phys. **55**, 476 (1984).
[6] U. Gomez, M. Leonhardt, H. Port, and H. C. Wolf, Chem. Phys. Lett. **268**, 1 (1997).
[7] M. Leonhardt, O. Mager, and H. Port, Chem. Phys. Lett. **313**, 24 (1999).
[8] S. R. Forrest, M. L. Kaplan, and P. H. Schmidt, J. Appl. Phys. **55**, 1492 (1984).
[9] T. Ogawa, K. Kuwamoto, S. Isoda, T. Kobayashi, and N. Karl, Acta Cryst. B **55**, 123 (1999).
[10] F. F. So and S. R. Forrest, Phys. Rev. Lett. **20**, 2649 (1991).
[11] E. I. Haskal Z. Shen, P. E. Burrows, and S. R. Forrest, Phys. Rev. B **51**, 4449 (1995).
[12] V. Bulović, P. E. Burrows, S. R. Forrest, J. A. Cronin, and M. E. Thompson, Chem. Phys. **210**, 1 (1996).
[13] V. Bulović and S. R. Forrest, Chem. Phys. **210**, 13 (1996).
[14] Z. G. Soos, M. H. Hennessy, and G. Wen, Chem. Phys. **227**, 19 (1998).
[15] M. H. Hennessy, Z. G. Soos, R. A. Pascal, and A. Girlando, Chem. Phys. **245**, 199 (1999).
[16] M. Hoffmann, K. Schmidt, T. Fritz, T. Hasche, V. M. Agranovich, and K. Leo, Chem. Phys. **258**, 73 (2000).
[17] M. H. Hennessy, Z. G. Soos, V. Bulović, and S. R. Forrest, Mat. Res. Soc. Symp. Proc. **488**, 171 (1998).
[18] M. Hoffmann and Z. G. Soos, Phys. Rev. B **66**, 024305 (2002).
[19] G. Mazur, P. Petelenz, and M. Slawik, J. Chem. Phys. **118**, 1423 (2003).
[20] R. Scholz, A. Yu. Kobitski, I. Vragović, G. Salvan, T. U. Kampen, D. R. T. Zahn, and H. P. Wagner, in: *Physics of Semiconductors 2002*, Proc. of the 26th Int. Conf. on the Physics of Semiconductors, Edinburgh, 29 July - 2 August 2002, Institute of Physics Conf. Ser. **171**, ed. by A.R. Long and J. H. Davies, Institute of Physics Publishing (Bristol 2002), P 266.
[21] A. Yu. Kobitski, R. Scholz, I. Vragović, H. P. Wagner, and D. R. T. Zahn, Phys. Rev. B **66**, 153204 (2002).
[22] A. Yu. Kobitski R. Scholz, D. R. T. Zahn, and H. P. Wagner, submitted to Phys. Rev. B (2003).
[23] R. Scholz, I. Vragović, A. Yu. Kobitski, G. Salvan, T. U. Kampen, M. Schreiber, and D. R. T. Zahn, in: Proc. Int. School of Physics "E. Fermi", course CXLIX: *Organic nanostructures: Science and applications*, ed. by V. M. Agranovich and G. C. La Rocca, IOS Press (Amsterdam 2002), p. 379 - 402.
[24] A. Djurišić, T. Fritz, and K. Leo, Opt. Commun. **183**, 123 (2000).
[25] I. Vragović, R. Scholz, and M. Schreiber, Europhys. Lett, **57**, 288 (2002).
[26] R. Scholz, I. Vragović, A. Yu. Kobitski, M. Schreiber, H. P. Wagner, and D. R. T. Zahn, phys. stat. sol. (b) **234**, 403 (2002).
[27] R. Scholz, A. Yu. Kobitski. T. U. Kampen, M. Schreiber, D. R. T. Zahn, G. Jungnickel, M. Elstner, M. Sternberg, and Th. Frauenheim, Phys. Rev. B **61**, 13659 (2000).
[28] K. Gustav, M. Leonhardt, and H. Port, Monatshefte Chemie **128**, 105 (1997).
[29] Summed over the A_g modes in Ref. [27] between 0.13 eV and 0.20 eV
[30] H. Froeb, unpublished.
[31] A. La Magna and R. Pucci, Phys. Rev. B **53**, 8449 (1996).
[32] A. S. Davydov, *Theory of Molecular Excitons*, Plenum Press (New York 1971).
[33] V. M. Agranovich and M. D. Galanin, *Electronic Excitation Energy Transfer in Condensed Matter* North-Holland (Amsterdam 1982).
[34] M. Wewer and F. Stienkemeier, Phys. Rev. B **67**, 125201 (2003).
[35] C. Kittel, *Quantum Theory of Solids*, John Wiley & Sons (New York 1963)
[36] A. S. Davydov and E. F. Sheka, phys. stat. sol. **11**, 877 (1965).
[37] D. Beljonne, J. Cornil, R. Silbey, R. Millié, and J. L. Brédas, J. Chem. Phys. **112**, 4749 (2000).
[38] D. Y. Zang, F. F. So, and S. R. Forrest, Appl. Phys. Lett. **59**, 823 (1991).
[39] L. D. Landau and E. M. Lifshitz, *Electrodynamics of Continuous Media*, Pergamon Press (Oxford 1984).
[40] R. Resta, Phys. Rev. B **16**,2717 (1977).
[41] A. D. Rakić and M. L. Majewski, J. Appl. Phys. **80**, 5909 (1996).
[42] R. Brendel and D. Bormann, J. Appl. Phys. **71**, 1 (1992).
[43] *Handbook of Mathematical Functions*, Editor: M.

Abramowitz and I. Stegun, Dover (New York 1965).

[44] T. U. Kampen, A. M. Paraian, U. Rossow, S. Park, G. Salvan, Th. Wagner, M. Friedrich, and D. R. T. Zahn, phys. stat. sol. (b) **188**, 1307 (2001).

[45] M. Friedrich, Th. Wagner, G. Salvan, S. Park, T. U. Kampen, and D. R. T. Zahn, Appl. Phys. A **75**, 501 (2002).

[46] R. Scholz, M. Friedrich, G. Salvan, T. Kampen, D. R. T. Zahn, and Th. Frauenheim, submitted to J. Phys. Cond. Matter (2003).

[47] M. I. Alonso, M. Garriga, N. Karl, J. O. Ossó, and F. Schreiber, Organic Electronics **3**, 23 (2002).

[48] M. Knupfer, T. Schwieger, J. Fink, K. Leo, and M. Hoffmann, Phys. Rev. B **66**, 035208 (2002).

[49] I. Vragović, thesis, Technische Universität Chemnitz (2003).

[50] R. Loudon, *The Quantum Theory of Light*, Clarendon (Oxford 1983), chapter 2.4.

[51] Handbook of Physics and Chemistry, 75th edition, CRC Press (Boca Raton 1994), p. **3**-207.

[52] A. Nollau, M. Hoffmann, K. Floreck, T. Fritz, and K. Leo, J. Appl. Phys. **87**, 7802 (2000).

[53] A. Yu. Kobitski, G. Salvan, H.-P. Wagner, and D. R. T. Zahn, Appl. Surf. Sci. **179**, 209 (2001).

[54] T. Hasche, T. W. Canzler, R. Scholz, M. Hoffmann, K. Schmidt, Th. Frauenheim, and K. Leo, Phys. Rev. Lett. **86**, 4060 (2001).

[55] G. Salvan, D. A. Tenne, A. Das, T. U. Kampen, and D. R. T. Zahn, Organic Electronics **1**, 49 (2000).